

POLITECNICO DI TORINO

Master Degree in Biomedical Engineering

*Prediction of Ultrasonic Wave Driven Conformational  
Dynamics of Amyloid Protein Assemblies By Molecular  
Modelling*



**Thesis Supervisor**

Prof. M. A. Deriu

**Co-Supervisors**

Prof. U. Morbiducci

**Candidate**

Marcello Miceli

ACADEMIC YEAR 2018-2019



# Table of contents

<b>ABSTRACT</b> .....	<b>1</b>
<b>1 INTRODUCTION</b> .....	<b>2</b>
<b>2 BIOLOGICAL BACKGROUND</b> .....	<b>4</b>
<b>2.1 Dementias and Alzheimer’s social and economic impact</b> .....	<b>4</b>
<b>2.2 Alzheimer</b> .....	<b>5</b>
2.2.1 Cholinergic hypothesis.....	6
2.2.2 Amyloid cascade hypothesis .....	6
2.2.3 Tau hypothesis .....	7
2.2.4 Excitotoxicity.....	8
<b>2.3 Amyloid <math>\beta</math> protein</b> .....	<b>9</b>
2.3.1 Structural polymorphism of amyloid .....	10
2.3.2 Amyloid peptide fibrillization.....	11
<b>2.4 Pharmacological approaches to treat Alzheimer’s disease</b> .....	<b>12</b>
2.4.1 Current pharmacological approaches: cholinesterase inhibitors and memantine .....	12
2.4.2 Potential future pharmacological approaches .....	13
<b>2.5 Ultrasound as a new nonpharmacological strategy to treat Alzheimer’s disease</b> .....	<b>14</b>
2.5.1 <i>In-vivo</i> Studies.....	14
2.5.2 <i>In-vitro</i> studies .....	15
<b>2.6 Computational studies</b> .....	<b>15</b>
<b>3 MATERIALS AND METHODS</b> .....	<b>17</b>
<b>3.1 Molecular modelling</b> .....	<b>17</b>
<b>3.2 Molecular Mechanics</b> .....	<b>17</b>
3.2.1 Potential energy function .....	18
3.2.2 Treatment of Bond interaction .....	18
3.2.3 Treatment of Non-Bond interactions .....	19
3.2.4 Periodic Boundary conditions.....	21
3.2.5 Potential Energy Minimization .....	22

<b>3.3</b>	<b>Computer Simulation method: Molecular Dynamics</b> .....	<b>23</b>
<b>3.4</b>	<b>Phase space and statistical ensemble</b> .....	<b>24</b>
3.4.1	Ensemble average, time average and ergodic hypothesis .....	24
3.4.2	Molecular Dynamics Implementation Scheme .....	26
<b>3.5</b>	<b>Rayleigh-Plesset equation</b> .....	<b>29</b>
3.5.1	Non-equilibrium all-atom molecular dynamics simulation of the bubble cavitation and application to dissociate amyloid fibrils .....	29
<b>4</b>	<b>MOLECULAR EFFECTS OF ULTRASOUNDS BY SIMULATING STABLE CAVITATION PHENOMENA WITH ATOMIC RESOLUTION</b> .....	<b>31</b>
<b>4.1</b>	<b>Introduction</b> .....	<b>31</b>
<b>4.2</b>	<b>Materials and methods</b> .....	<b>32</b>
4.2.1	Amyloid $\beta$ U-shape model .....	33
4.2.2	System Setup, Configuration and Validation.....	33
4.2.3	Ultrasound setup .....	33
<b>4.3</b>	<b>Results</b> .....	<b>34</b>
4.3.1	Conformational Analysis .....	34
4.3.2	Structure stability analysis .....	37
<b>4.4</b>	<b>Discussion</b> .....	<b>41</b>
<b>5</b>	<b>ULTRASONIC WAVES EFFECT ON B-AMYLOIDS CONFORMATIONAL DYNAMICS BY NON-EQUILIBRIUM MOLECULAR DYNAMICS SIMULATION</b> .....	<b>43</b>
<b>5.1</b>	<b>Introduction</b> .....	<b>43</b>
<b>5.2</b>	<b>Materials and methods</b> .....	<b>44</b>
5.2.1	Amyloid $\beta$ S-shape models .....	44
5.2.2	System setup and Configuration .....	45
5.2.3	Order parameter analysis .....	46
<b>5.3</b>	<b>Results</b> .....	<b>46</b>
5.3.1	Analysis of structure stability for 2MXU .....	46
5.3.2	Analysis of structure stability for 5OQV .....	51
<b>5.4</b>	<b>Discussion</b> .....	<b>55</b>

**6 CONCLUSIONS .....57**

**7 ACKNOWLEDGMENT .....58**

**8 BIBLIOGRAPHY .....59**

## Abstract

Dementia defines a group of chronic degenerative diseases that nowadays affects 46.8 million of people, a number that in the next thirty years will increase to 131.5 million. Alzheimer's disease accounts approximately 60% of all dementias. This illness is characterized by memory and cognitive deterioration. Different theories have been proposed to explain mechanism underlying the pathology and among these, the so called "amyloid cascade hypothesis" is the most accredited one: the misfolding of a protein called  $\beta$ -amyloid and its successive accumulation into plaques in proximity of neurons degenerates in memory loss and confusion. The primary aminoacidic sequence of  $\beta$ -amyloid is composed of 42 residues. In literature two conformations for  $\beta$ -amyloid 1-42 have been observed, called U-shape and S-shape. Molecular dynamics simulations showed that S-shape conformation is more stable than U-shape. Nowadays, pharmacological treatments proposed to counteract the pathology act reducing the symptoms instead of focusing on the causes, moreover the use is related to relevant side effects. Alternative pharmacological treatment has been proposed, to counteract the pathology, acting on the causes however no one have shown to be promising. Ultrasound techniques are widely used in medicine, due to their relative safety. Experimental studies confirm qualitatively the possibility of disassembly amyloid aggregates driven by ultrasound, related to the phenomenon of bubble stable cavitation. However, the short time scale of the phenomenon limits experimental measures. Computational modelling and in particular, molecular dynamics techniques, allow to observe nanoscale level phenomena involving biological systems such as proteins. In this work we implemented an ultrasound simulator computational code to be coupled with classical molecular dynamics engines, such as GROMACS. Starting from several inspiring literature previous works on the field, the effect of ultrasonic waves applied to a molecular system was simulated by adding to the mentioned system a number of dummy bubbles with van der Waals radius varying as function of time, proportionally to an ultrasonic pressure wave. The code was employed to investigate stability of amyloid fibrils with respect to their architecture and results have been compared with recent literature. Results, in agreement with previous works, highlighted higher mechanical properties for S-shape conformation of  $\beta$ -amyloid fibrils when compared with U-shape. Moreover, the research highlights the importance of N-terminal residues, 1 to 17, in the stability of the above mentioned amyloid fibrils. To conclude, the algorithm implemented in this research might be further employed to explore alternative treatment to neurodegenerative diseases based on synergic effect between chemicals and ultrasound. Moreover, the implemented code could be, in future, configured as a new tool to investigate proteins' stability features as dependent on environmental conditions.

# 1 Introduction

The group of neurodegenerative diseases called dementia, represent a social and economic burden of our century, affecting 46,8 million people worldwide. Moreover, it is believed that this illness will affect 131,5 million people in the next thirty years. The most diffused type of dementia is Alzheimer's disease, that accounts for 60 % of all patients affected by dementia, characterized by memory and cognitive deterioration. In addition, the progression of this illness is related to high costs for society and emotional burden for families. For these reasons, dementia and mainly Alzheimer represents an open and wide field of research for drugs development and treatments. Many hypotheses have been proposed to explain process that leads to Alzheimer. The so-called Amyloid cascade hypothesis has emerged has one of the most promising. In accord to this theory, misfolding of the extracellular  $\beta$ -amyloid ( $A\beta$ ) protein and further aggregation into extracellular plaques leads to memory loss and confusion.  $A\beta$  structure has been widely studied in order to understand causes that lead to aggregation and thus find strategies to counteract this phenomenon. The group of peptides that belong to the family of  $A\beta$  varies from 37 to 49 residues. Among these the most abundant is the  $A\beta_{40}$  while the most toxic is the  $A\beta_{42}$  which showed higher tendency to aggregation. Moreover, while  $A\beta_{40}$  showed a univocal U-shape conformation, recently it has been proposed that  $A\beta_{42}$  can organize into two architectural conformations, the U-shape and the S-shape. Many compounds have been developed in order to counteract  $A\beta_{42}$  aggregation, however some of that have showed to be toxic while other have showed to be not effective. Ultrasounds have been recently proposed as an alternative non-pharmacological strategy to contrast  $A\beta$  accumulation. However, while in vitro and in vivo studies have shown its effectiveness, experimental observation results a challenge. Indeed, state of art, does not account techniques with appropriate characteristic in terms of time and length resolution. Computational techniques nowadays have exponentially grown due to great improvement in computer hardware and software. Computational Molecular Modelling is emerging as an elective tool to investigate molecules, capable to describes atomic behaviour within nanoseconds of resolution.

The aim of the present work is to use tool provided from Molecular Modelling to elucidate the effect of ultrasound on  $A\beta_{42}$  protein aggregates. Inspired from literature a method will be implemented to be used with classical molecular modelling engines, GROMACS. Then further analysis will be performed on different architecture of  $A\beta_{42}$ , to highlight dynamics and mechanics of different conformations and how that affects  $A\beta_{42}$  stability.

Work will be organized as follows:

**Chapter 1** is the present introduction where technical and biological background is summarized and the aims of this work will be exposed.

**Chapter 2** biological and technical background will be introduced. From biological point of view, an overview on dementia and mainly on Alzheimer disease will be provided. Focusing on A $\beta$  structures and characteristics. Moreover, actual pharmacological strategies will be discussed, along with their limitations. Ultrasound, as a new strategy, will be introduced, within his relation to the phenomenon of bubble cavitation. At the end technical background on computational studied for ultrasound molecular dynamics simulation and on A $\beta$  properties related to its polymorphism will be investigated.

**Chapter 3** is an overview of the methods used in this work. Molecular Modelling will be introduced, with a general description of Molecular Mechanics and Molecular Dynamics, focusing on theoretical and physical aspects; then Rayleigh-Plesset equation will be introduced. To conclude a method to perform ultrasound Molecular Dynamics simulation will be discussed.

**Chapter 4** inspired from literature, a code to perform ultrasound molecular dynamics simulation will be developed and validated on results reported from literature. Moreover, dynamics and mechanics of protein unfolding, for A $\beta$ 42 U-shape model, driven by ultrasound will be discussed. The focus on effect of secondary structures and causes that lead to disaggregation will then follow.

**Chapter 5** is devoted to describes the effect of destabilization for A $\beta$ 42 S-shape models driven by ultrasound. As done in previous chapters, analyses of dynamic and mechanic of destabilization will be performed. Moreover, investigation was carried out for two model for A $\beta$ 42 S-shape, to clarify the effect of N-terminal residues on protein stability.

**Chapter 6** results from chapter 4 and 5 will be summarized to have an overall overview on the effect of ultrasound driven destabilization for A $\beta$ 42.

## 2 Biological background

### 2.1 Dementias and Alzheimer's social and economic impact

Dementias defines a group of diseases characterized by a chronic degenerative condition related to a loss of mental functions such as orientation, memory language and visual recognition. More than 90% of people that suffer from dementia are older than 65 years, so ageing has been indicated as the most robust risk factor for the disease [1]. The World Alzheimer Report estimates 46.8 million the number of people affected by dementia in 2015, with an increase that can reach up to 131.5 million in 2050 [2]. The average dementia care costs for one patient per year in Europe are € 32,506 [3]. Classification of dementias is based on their pathologies, which are characterized by an accumulation of abnormal aggregates of protein in neurons and glia, extracellular compartment and in vulnerable regions of the brain [4]. The main dementias syndromes are Alzheimer disease, Frontotemporal dementia, Lewy body dementia, Prion disease and Vascular dementia [5]. The most common disease in people affected from dementia is Alzheimer's disease (AD) that accounts approximately for 60% of all dementias. Nowadays Alzheimer's disease in Europe impacts with a higher average cost, compared to the mean care costs of dementias diseases, that is of 46,752 € [6].

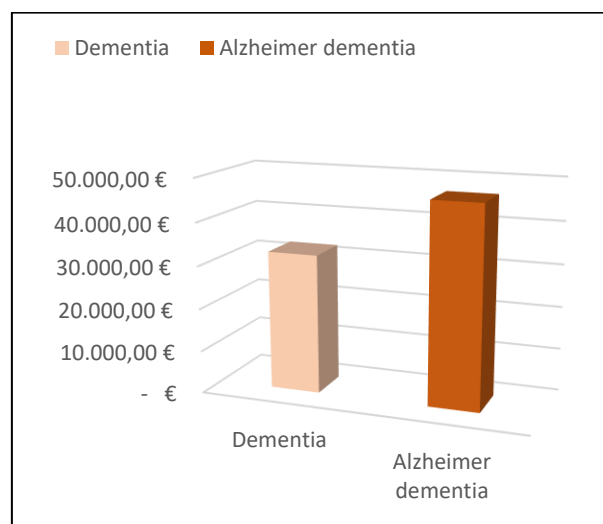


Figure 1: average cost for a patient for a year, the average for a patient affected by dementias (on left), focus for patients affected by Alzheimer's disease dementia (right)

Dementia does not only represents a relevant cost for the community, but its burden of dementia for caregivers is also often a cause of considerable emotional stress, especially for those who are informal caregivers that look after a relative. The reduced ability of people to carry out daily activities and communicate can be especially challenging for those around them, placing both physical and mental

strains on carers. In fact it has been shown that caregivers are more likely to suffer from anxiety and depression [7].

## 2.2 Alzheimer

Alzheimer's disease (AD) is the most common type of dementia, which is a progressive and neurodegenerative disorder characterized by memory and cognitive deterioration, impairment in daily activity and a wide type of behavioural disturbance and neuropsychiatric symptoms. Alzheimer's classical features are deterioration of language, amnesic type of memory impairment, visuospatial deficits [8]–[10]. AD is characterized by the presence of senile plaques, founded between neurons in the brain and neurofibrillary tangles, which develop inside neuronal cells [11].

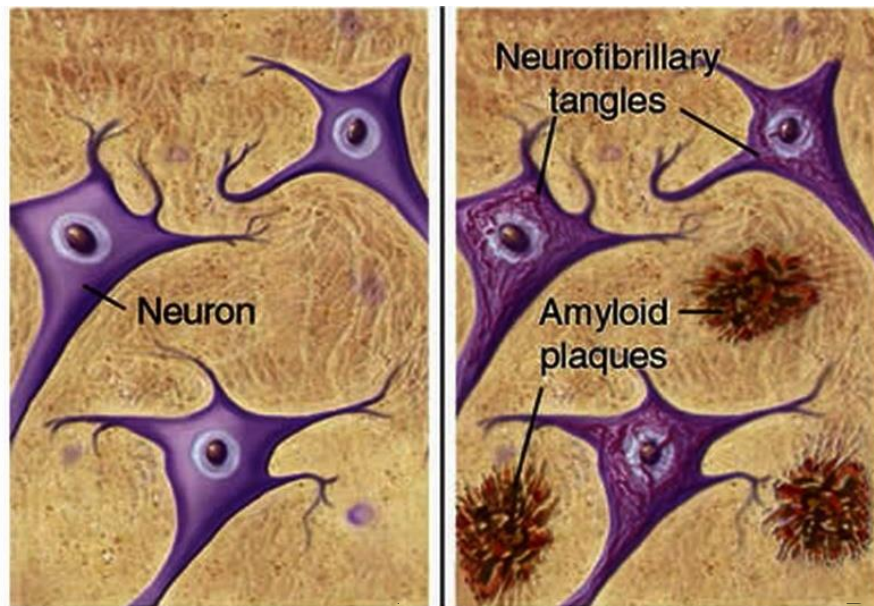


Figure 2: Differences between normal neurons (A) and neurons of AD patient (A). The two principal AD hallmarks are beta-amyloid plaques, which originates senile plaques, and hyperphosphorylated tau protein, which forms neurofibrillary tangles.

The diagnosis of AD is a challenging task and there is not a univocal testing strategy, physicians assisted by neurologist and geriatricians try to help the diagnosis through a wide range of approaches and tools [5], [12]:

- conducting physical and neurological examinations and cognitive tests;
- going through the medical and family history, including the history of cognitive and behavioural changes and the psychiatric history;
- asking the relatives and close people to provide input about a mutation in behaviour and thinking skills;

- some circumstances need the use of brain imaging to find out if the individual has high level of hallmarks such beta-amyloid
- make withdrawals of body fluids to find out the presence of high concentrations of biomarkers such beta-amyloids, tau and P-tau in spinal fluid

Even though AD has been described in ancient writings over the human history (e.g., “Be kind to your father, even if his mind fails him.” – Old Testament: Sirach 3:12), its clinical story is fairly recent: Alzheimer published his case study in 1907 and from the 1980s researches begun to accelerate [13]. Despite the high efforts to understand the causes, there is not a univocal hypothesis on the mechanism underlying the pathology of AD. The most accredited theories are cholinergic hypothesis, Amyloid cascade hypothesis, Tau hypothesis, and Excitotoxicity.

### **2.2.1 Cholinergic hypothesis**

In 1970s, consequently to an observation of a cholinergic paucity in the brains of AD patients, mediated by deficits in the enzyme choline acetyltransferase, this first hypothesis came out [14]. This observation, linked to the simultaneous discovery of the role of acetylcholine in learning and memory, led to the well-known Cholinergic hypothesis. Strategies developed to contrast this phenomenon regards the attempt to increase the cholinergic activity. Cholinesterase inhibitors potentiate cholinergic transmission acting on the cholinesterase enzyme, responsible for the breaking down of acetylcholine at the synaptic cleft. However, it has been shown that cholinergic depletion is one of the latest features of the neurodegenerative cascade.

### **2.2.2 Amyloid cascade hypothesis**

The amyloid cascade hypothesis started to attract the scientific community around the 1990s. The amyloid hypothesis proposes that misfolding of the extracellular  $\beta$ -amyloid ( $A\beta$ ) protein gathered in plaques degenerates in memory loss and confusion [15]. The  $A\beta$  peptide derives from the proteolysis of a large glycoprotein named amyloid precursor protein (APP). APP is physiologically cleaved from secretase enzyme, however atypical mutation of  $\gamma$  and  $\beta$  secretases can lead to the production of toxic  $A\beta$  [16] ( ). First step of the cascade is an abnormal concentration of  $A\beta$ , due to an enhanced production or a reduced clearance from the brain. A positive feedback process is then triggered, indeed  $A\beta$  accumulation increases oligomer formation, which alters synaptic functions. Together increased concentration of  $A\beta$  monomers starts to aggregate into fibrils. Amyloid plaques acts have a deposit of  $A\beta$  peptide leading to an inflammatory response. All these events alter ionic

homeostasis and cause oxidative stress of neurons. Cascade culminates into neural loss and synaptic damage, and finally to the pathological hallmarks of AD [17], [18].

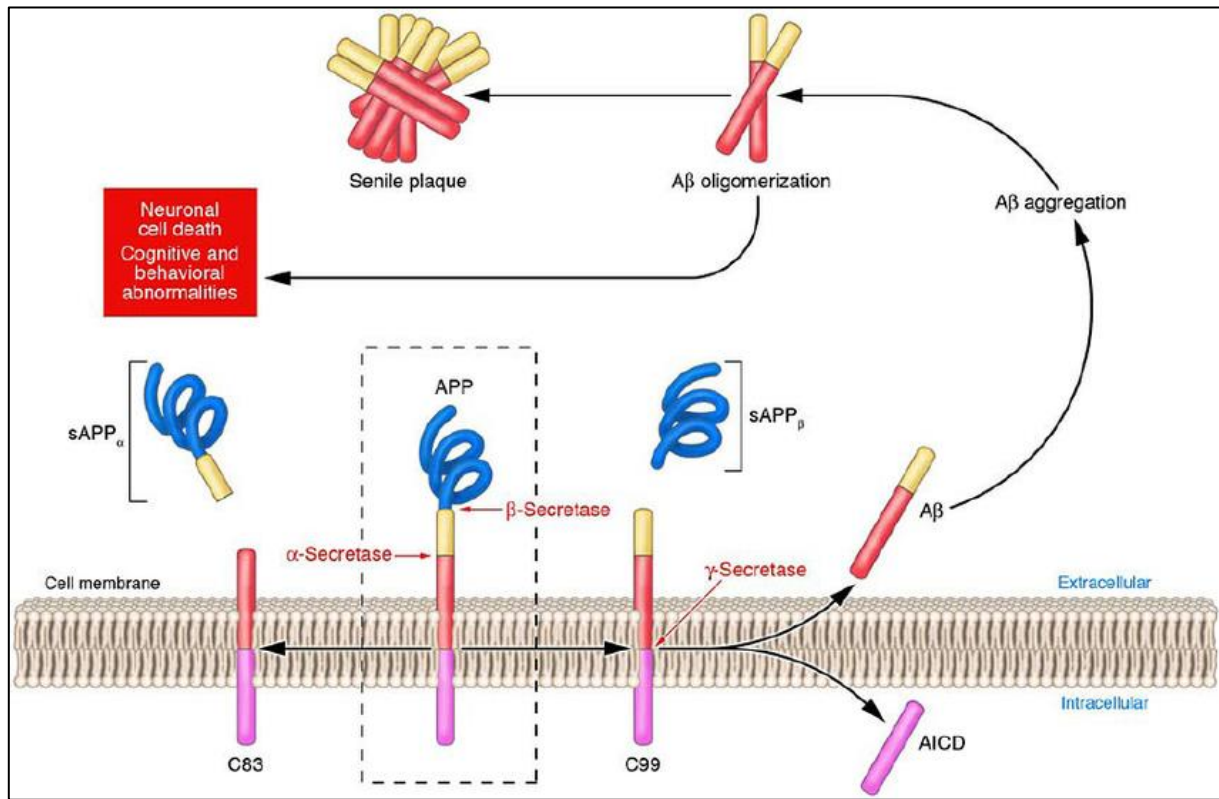


Figure 3: Amyloid cascade hypothesis that Aβ peptide derives from the proteolysis of a large glycoprotein the amyloid precursor protein (APP).

### 2.2.3 Tau hypothesis

Tau hypothesis is strictly related to the amyloid cascade hypothesis. Tau proteins are physiologically expressed in neural cells and acts for stabilizing microtubules in the cell cytoskeleton [19]. It has been hypothesized that hyperphosphorylation of tau proteins leads to an accumulation on these molecules into masses that forms neurofibril tangles. These aggregates interact with the cells preventing their normal functions, indeed loss of Tau stabilizing function can lead to abnormalities in cytoskeleton structure with further alteration of axonal transport leading to synaptic dysfunction and then neurodegeneration [20]. It has been proposed that neurofibrillary tangles, composed of tau-p proteins, may be triggered by Aβ plaques and are strongly correlated with neural loss and cerebral atrophy. Additionally, it has been observed that aggregates of Tau can improve the production of Aβ via a feedback loop mechanism [21].

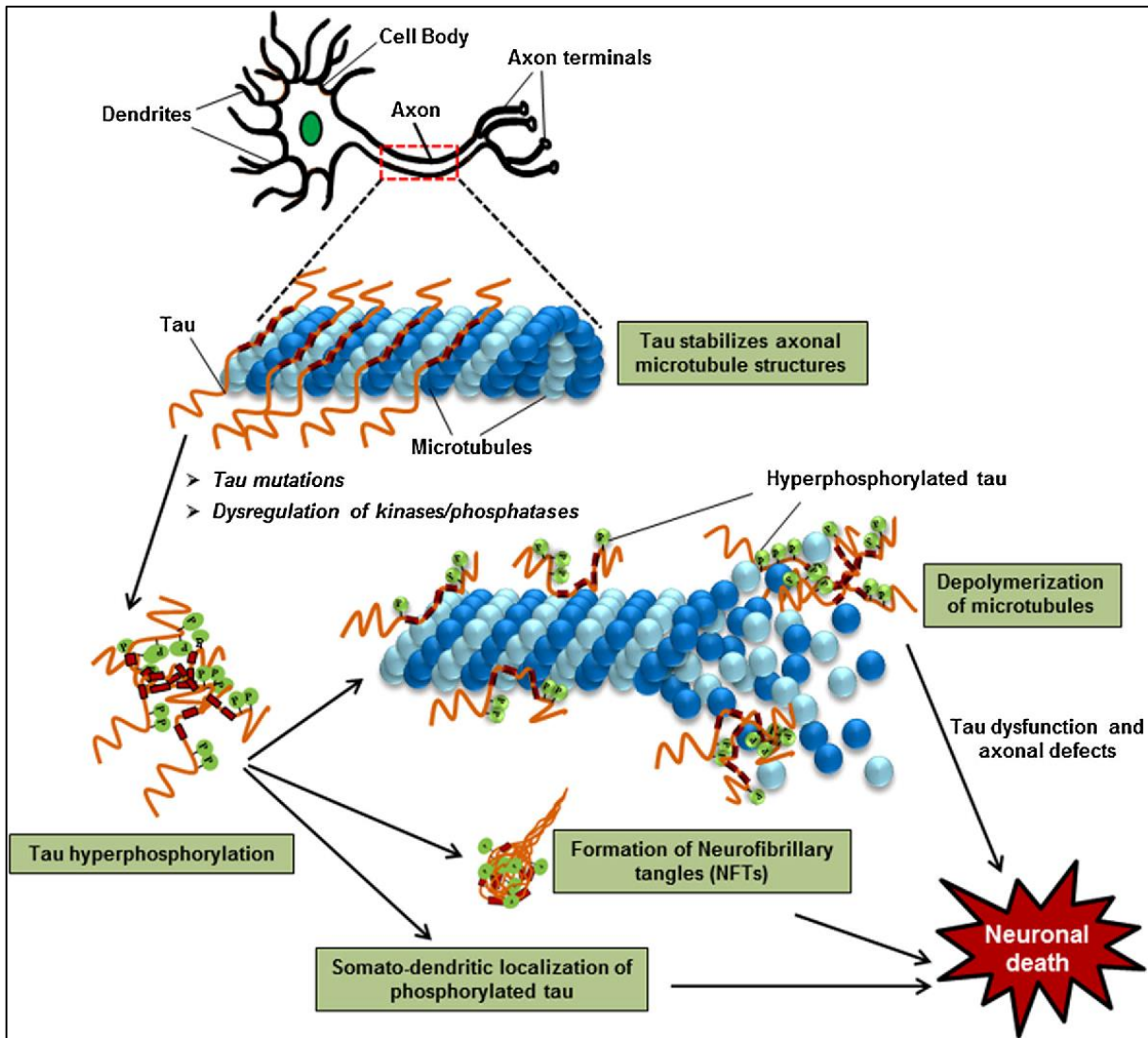


Figure 4: Hyperphosphorylation of tau protein and successive aggregation in neurofibril tangles [22]

#### 2.2.4 Excitotoxicity

Excitotoxicity is defined as an overexposure to the neurotransmitter glutamate or overstimulation of its receptor N-methyl-D-aspartate (NMDA). This phenomenon has been partially correlated to the neuronal loss of AD. It has been suggested that loss of cholinergic neurons, with consequential disproportionate influx of calcium into cell, is related to this phenomenon. There is a link between Amyloid hypothesis and excitotoxicity: it has been shown in vitro experiment that A $\beta$  generated oxidative stress and increased intracellular Ca $_2^+$  enhancing glutamate-mediated neurotoxicity [23], [24]. Moreover, additional experiments reported that A $\beta$  can increase excitotoxicity by and augmented NMDA activity[25]. Finally, it has been reported that excessive NMDA activity increases the hyperphosphorylation of tau, which contributes to neurofibrillary tangles [26].

## 2.3 Amyloid $\beta$ protein

The  $A\beta$  peptide is proteolyzed from a transmembrane protein APP, expressed in a wide range of tissues especially in the synapses of neurons. APP consists of a single membrane-spanning domain, a large extracellular glycosylated N-terminus and a shorter cytoplasmic C-terminus. Different isoforms are expressed in nature and the number of residues can vary from 695 to 770 amino acids. APP is proteolyzed from  $\alpha$ -secretases or  $\beta$ -secretases, and then from  $\gamma$ -secretases to produce a peptide that can be built by 37 to 49 residues [27]. APP is processed through two pathways: nonamyloidogenic and amyloidogenic. The  $\alpha$ -secretases are the enzymes that start the non-amyloidogenic pathway while  $\beta$ -secretases start the amyloidogenic pathways; both processes release membrane-tethered  $\alpha$ - or  $\beta$ - C-terminal fragments (CTFs). The  $\alpha$ -secretase splits APP structure releasing from the cell surface sAPP $\alpha$  and a C-terminal fragment of 83 amino acids (C83),  $\beta$ -secretase cleavage results in sAPP $\beta$  a 99 amino acids C-terminal fragment C99 [28]. Then, further process of cleavage by  $\gamma$ -secretase process the  $\alpha$ - or  $\beta$ -CTFs producing respectively P3 or  $A\beta$  [29] (Figure 5).

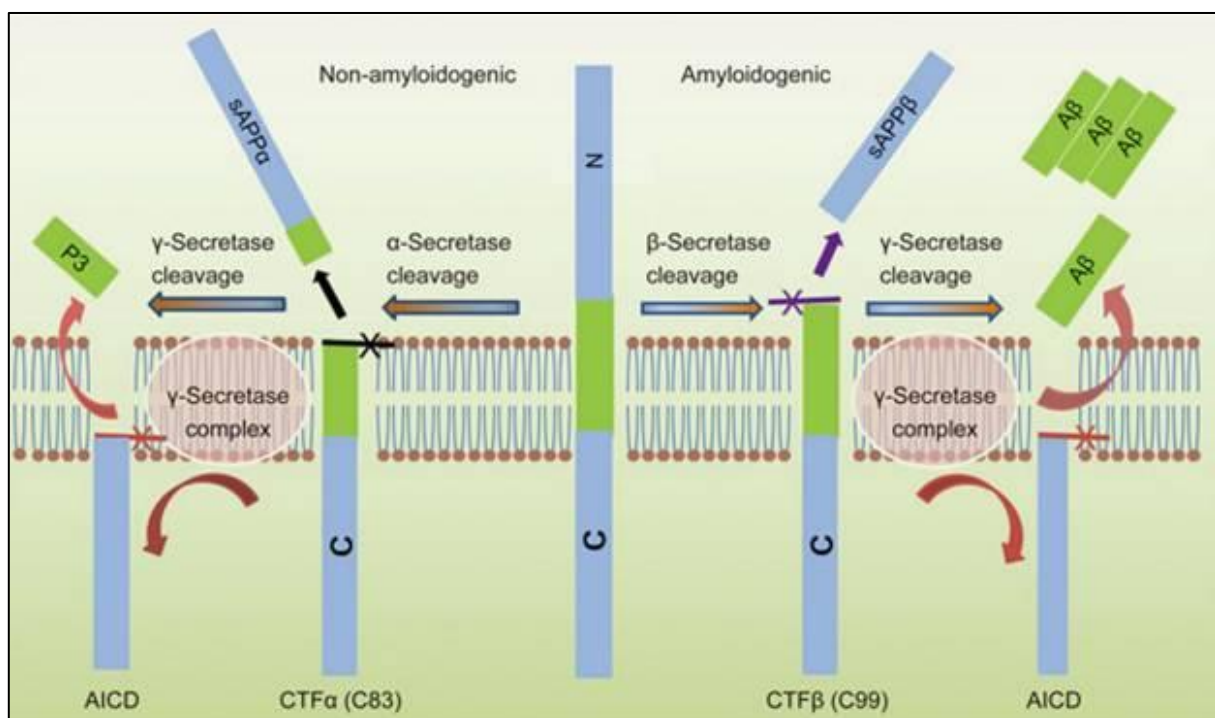


Figure 5: cleavage pathways of APP in the human body, on the left non-amyloidogenic pathway and on the right the amyloidogenic pathway that results in  $A\beta$  monomers [30].

The primary amino acid sequence, Figure 6, of the 42- $\beta$ -Amyloid ( $A\beta$ 42) is:

$N - DAEFRHDSGYEVHHQKLVFFAEDVGSNKGAIIGLMVGGVVIA - C$  [31].

The group of peptides that belongs to the family of A $\beta$  varies from 37 to 49 residues. Recent Nuclear magnetic resonance (NMR) studies highlighted that A $\beta$  peptide (1-28) folds into the  $\alpha$ -helical structure and it converts in membrane-like media into  $\beta$ -sheet. That probably happens during first phases of amyloid formation in Alzheimer's disease. In this peptide, the side chains of histidine-13 and lysine-16 are at the same face of the helix. A $\beta$  (1-40) shows an  $\alpha$ -helix conformation among residues 15 and 36 within which the residues 25-27 include a kink, moreover the peptide is unstructured between the chiefly polar residue 1 and 14, that are more likely to be solvated by water. It has been shown that the deprotonation of two acid residues in the helix drives a helix-to-coil switching that precedes the aggregation [32] (Figure 6). The A $\beta$  monomers assemble in a wide way, including oligomers, protofibrils, and amyloid fibrils. The oligomers are soluble and may spread across the brain, while the fibrils are bigger and insoluble and can assemble into amyloid plaques.

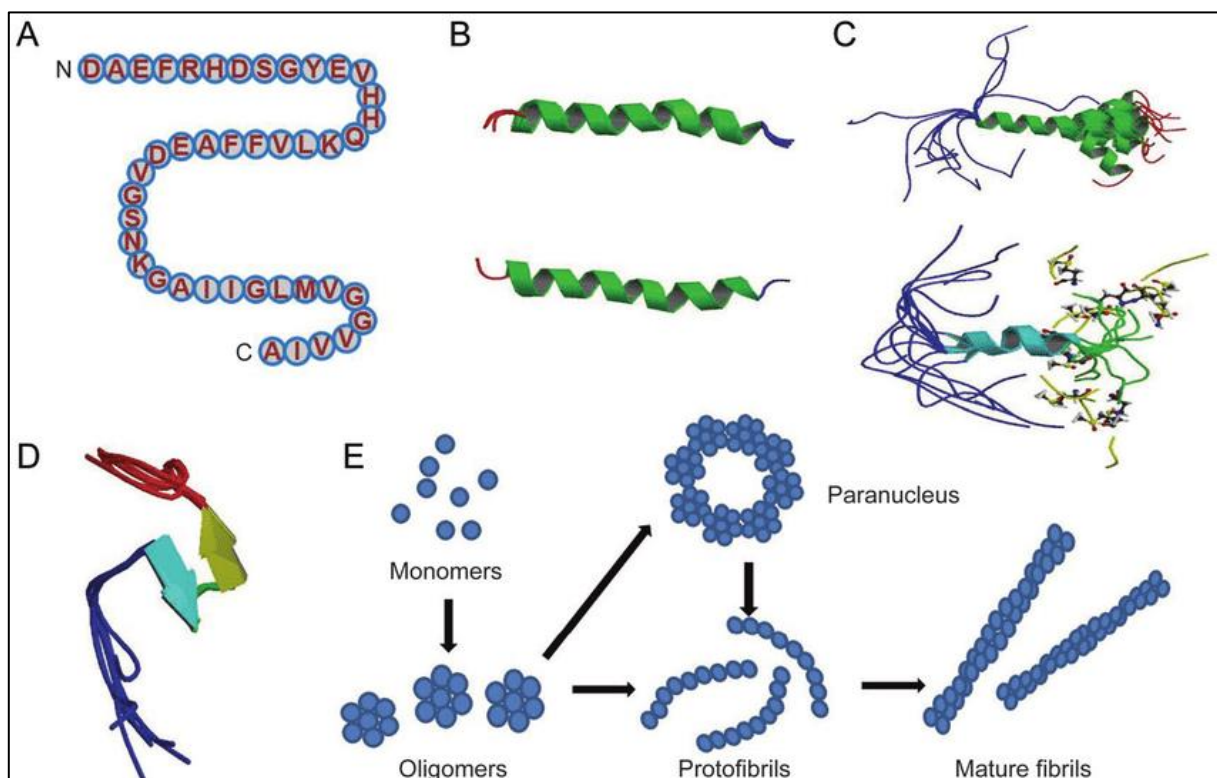


Figure 6: A $\beta$  peptide derives from the proteolysis of APP and different isoform that varies from 39 to 49 residues are present in nature. (A) primary aminoacidic sequence of A $\beta$ 42, (B) structure of A $\beta$ 1-28, which form an alpha-helical structures, (C) solute structure of monomer A $\beta$ 40 that forms an alpha-helical structures between residues 15-36 whit a hinge or a kink between residues 25-27, (D) collapsed coil structure formed by A $\beta$ 10-35, one quarter of the surface is hydrophobic and the coil structure is meta-stable, this characteristic may lead to a global conformation rearrangement and formation of beta-sheet structures that cause fibrillation, (E) hypothesis of pathways that can lead to the formation of oligomers and then to fibrillation [30].

### 2.3.1 Structural polymorphism of amyloid

Most frequently the principal components in amyloid plaques are A $\beta$  peptides 1-40 (A $\beta$ 40) and 1-42 (A $\beta$ 42). It has been proposed from NMR studies that these two molecules present different

conformational states, a more structured  $\beta$ -hairpin that decreases the C-terminal flexibility has been observed in A $\beta$ 42, which may be responsible of the superior propensity of A $\beta$ 42 than A $\beta$ 40 to form amyloids. The NMR studies on A $\beta$ 40 structure suggested a U-shape motif where two  $\beta$ -strands are formed from the two chains connected by a loop region. A $\beta$ 42 shows not only stability in U-shaped conformation but also for an S-shaped structure, characterized by three  $\beta$ -stands [33]–[35]. The U-shaped conformation is constituted by two strands (the residues involved are V18-S26 and I31-A40) stabilized by salt bridges between residues D23-K28 and H-bonds inter chains [34]. More recently it has been shown that there is the possibility to have an S-shaped conformation for the A $\beta$  molecule [36]–[38], the N-terminal strand  $\beta$ 1 (residues V12-V18), middle strand  $\beta$ 2 (residues V24-G33) and C-terminal strand  $\beta$ 3 (residues V36-V40). Although A $\beta$ 40 and A $\beta$ 42 are different only for two residues the S-shaped conformation is not stable for the first peptide [39]. The first hypothesis for this difference was the absence of A42 in A $\beta$ 40, that in A $\beta$ 42 creates a salt-bridge between the side chain of K28 and the main chain in which the residue is [36]. Another hypothesis can be the presence of hydrophobic contact existing in the C-terminal residues I41 and A42 of A $\beta$ 42 that lacks into A $\beta$ 40 [40].

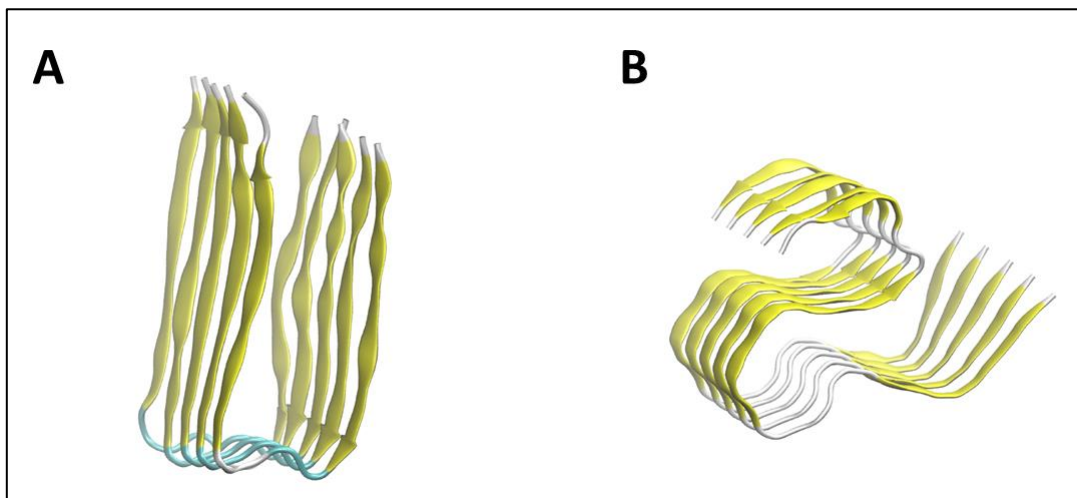


Figure 7: 5 chains Amyloid $\beta$  1-42 models: (A) U-shape model from PDB:2BEG [34]; (B) S-Shape model from PDB:2MXU[36].

### 2.3.2 Amyloid peptide fibrillization

The amyloid cascade hypothesis is based on the idea that A $\beta$  monomers tend to aggregate into oligomers and fibrils that leads to neurotoxicity and dementia. It has been shown that in a normal condition nearly 80% of amyloids in the human brain are present in the form of A $\beta$ 40 while in abnormal condition the concentration of A $\beta$ 42 increases and tends to aggregate. Moreover, A $\beta$ 42 has shown a faster aggregation kinetic and higher a neurotoxicity compared to A $\beta$ 40 [41]. A nucleation grow mechanism has been suggested to explain the fibril formation; in fact, initially an original

unfolded state of A $\beta$  shows slow transition into a partially folded state ( $\beta$ -sheets). Firstly, phase of folding dynamics is slow. Subsequently, hydrophobic interaction and hydrogen bonding between partially folded units start the aggregation of monomers and form paranucleus; then a higher-order structure called protofibril is formed by self-association. Then during the elongation phase, protofibrils are self-assembled to form long fibrillar aggregates [42] (Figure 6E). A wide number of pathways may lead to an aggregation of the peptide. Originally, studies supposed that the monomers were organized in a regular manner, called *cross  $\beta$*  pattern, where adjacent proteins are folded in an anti-parallel way inside the fibril lattice [43]. Then, subsequent research discovered that peptide chains of  $\beta$ -strands segments run perpendicularly to the long fibril, with intermolecular hydrogen bonds of  $\beta$ -strands organized in a *cross  $\beta$*  pattern, that run parallel to the fibril axis [44].

## **2.4 Pharmacological approaches to treat Alzheimer's disease**

AD represent a challenge also for the treatment and nowadays drugs act on the symptoms. Today the approved drugs treatment for AD accounts to Acetylcholinesterase inhibitors (AChEI) rivastigmine, donepezil, galantamine, and N-methyl-D-aspartate (NMDA) receptor antagonist memantine. These drugs, that are the only commercial available products, even if have shown to may improve cognitive and behavioural outcomes, they have a modest and controversial clinical impact [45]–[47]. In the last decade much effort has been focused on finding a way to disease modify-drugs that change the progression of the disease, instead of reducing the symptoms. Until now, different strategies have been proposed as an alternative to the current treatments with the aim of targeting the disease instead of the symptoms. The principal alternative treatments are anti-amyloid therapy, immunization, monoclonal antibodies and tau targeted therapy. However, any effective alternative pharmacological treatment has not been found yet [48].

### **2.4.1 Current pharmacological approaches: cholinesterase inhibitors and memantine**

The first generation of AChEI was tacrine, limited for the hepatotoxic side effects [49]. After the tacrine, the second generation of drugs come out, rivastigmine, galantamine and, probably the most widely used, donepezil. While rivastigmine acts both on butyryl cholinesterase (BuChE) and AChE, galantamine inhibits selectively AChE and does an activity as a modulator of nicotinic acetylcholine receptors (nAChRs) and donepezil acts selectively by inhibiting AChE [50]. These three drugs show the same results in terms of efficacy; thus, prescription is based on individual patient tolerance, cost and physician experience. The side effects that characterize these drugs are gastrointestinal, muscle cramp and fatigue; moreover, before a subscription of AChEI, all patient should have an electrocardiogram because of the related risk of conduction abnormalities. Average effects on

function and cognition are modest [51], showing variability in response rates, with a small proportion of patients, around 20%, that shows large benefits and 33% that shows no benefits.

Memantine is licensed in moderately to severe state of AD; it acts in two ways, as antagonist at NMDA receptors and as neuroprotector [52]. This drug is generally more tolerated than AChEI having less side effects; although headache, dizziness, somnolence, hypertension and constipation can occur.

Even if AChEI and NAMD inhibitors represent the current available therapies for AD, they show small overall effect and do not alter the progression of the original neurodegenerative process. Probably the actual drugs act too far downstream in the process that cause AD; For this reason, alternative strategies have been proposed to target the pathological process ‘upstream’ [53].

#### **2.4.2 Potential future pharmacological approaches**

In the last decade much effort has been involved in finding new strategies to discover disease-modifying drugs, which change the course of the disease rather than act on symptoms.

The first class of therapy is the anti-amyloid, that is based on the amyloid cascade hypothesis, which aims to alter the disease course targeting the amyloids or either the  $\beta$ -secretases or  $\gamma$ -secretases [54].

Another proposed strategy is the immunization against  $A\beta$  with the agent AN 1792. However, it has been stopped because of cases of meningoencephalitis in 6% of subjects [55]. Also, passive immunization with intravenous immunoglobulin containing  $A\beta$  has been tested and in phase II of trials has shown to be potentially efficacious and safe; however in phase III studies found no evidence for decelerating development of AD [56].

Monoclonal antibodies have been tested as a novel strategy and different formulation underwent trial phases. Solanezumab and bapineuzumab, two monoclonal antibodies to  $A\beta$ , showed to reduce the rate of amyloids during phase III of trial; however no cognitive or functional effects has been shown despite these showed to engage their target [57]–[59].

Also, a strategy based on the Tau hypothesis has been considered. The latter proposes agents to prevent hyperphosphorylation as well as those targeting microtubule aggregation and stability [60]. It has been proposed valproic acid and lithium as an anti Tau aggregating agent but randomised controls showed inconsistent results [61].

## ***2.5 Ultrasound as a new nonpharmacological strategy to treat Alzheimer's disease***

Given the results obtained with the pharmacological approach, alternative non-pharmacological strategies have been investigated in literature and ultrasound strategies arises as a promising one [62]. Ultrasounds (US) techniques are widely used in medicine for many applications that includes imaging and treatment. One of the main benefits of US is that they do not involve ionizing radiations, thus is it possible to perform long expositions also on patients at risk, as pregnant women [63]. US are acoustic waves whit frequency higher than 20 kHz; for medical application the frequency range usually goes from 1 to 15 MHz, while for imaging higher frequency and intensity are used, instead for treatment higher intensity and lower frequency are required [64]. The application in therapeutic US can be approximately categorized as thermal or non-thermal. While the thermal application includes physiotherapy and ablation of tissue, non-thermal application consists in the use of pulsed US to induce microbubble-mediate opening of Blood Brain barrier (BBB). Additional strategies are in phase of developing for neurological applications, including clearance of protein aggregates. These strategies employed an innovative technique called Focused Ultrasound (FUS), which uses multiple focalized USs to treat areas of a 5 mm of diameter and 10 mm of length. This process is based on mechanical and thermal effects, mostly produced by cavitation, a phenomenon that arise in liquid systems under the influence of pressure. In response to a mechanical force, water inside the environment, under ultrasonic excitation, contracts and expands, developing microbubbles that can suddenly collapse or change in shape harmonically [65]. An alternative approach to FUS is called Scanning ultrasound (SUS), in which the treatment is applied over the entire skull.

### ***2.5.1 In-vivo Studies***

Ultrasounds have been initially employed to enhance the blood-brain barrier (BBB) permeation in order to develop new drug delivery strategies; it has been also observed that ultrasounds themselves reduce the amount of plaques [66], [67]. In literature studies on TgCRND mice models are reported, in which a reduction of 20% of amyloids plaque and a partial restoring of memory related to a FUS treatment are shown. Leinenga & Götz studied the effects of scanning ultrasound (SUS) on mouse model APP23: they observed, during 6-weeks treatment, a reduction of plaques size comparable to that achieved by other methods that use SUS and therapeutic agent combined [62]. Moreover, the authors highlighted the role of microglia: comparing SUS-treated mice they observed that microglia fragmented and engulfed significantly more quantity of A $\beta$  plaques in respect to the sham case, that consists in only FUS without drug, used for comparison. While previous reported literature shows

how US can be applied to remove insoluble plaques of protein aggregates, factors that explain the in vivo results have to be established [68].

### **2.5.2 *In-vitro* studies**

Understanding the causes that lead to the formation of insoluble fibrils, and therefore to the AD, is fundamental to develop techniques that can counteract this phenomenon in a targeted way; in addition investigating how ultrasounds could act on fibrils causing defibrillation could lead to innovative technique to treat the AD patients. In literature, have been performed in-vitro study on ultrasonication of A $\beta$ 40: it shows a dual behavior of amyloids monomers exposed to acoustic waves, over specific conditions of concentration the agitation promotes the nucleation of fibrils, on the other hand under a critical concentration the ultrasonication accelerate depolymerization [69]. The authors explained the polymerization and depolymerization phenomena adducing the cause on strong shearing forced exerted on the fibrils due to solvent flow and driven by cavitation ultrasonication-dependent; they also propose that the concentration is the parameter that triggers the opposite behaviour. The short time scale of this events limits experimental in vitro observation of this phenomenon. Moreover, analytical theory is tough due to the non-linear non equilibrium phenomenon. Therefore, molecular dynamics (MD) studies have been performed to understand the process at the molecular level.

## **2.6 *Computational studies***

Computational methods and mainly Molecular Dynamics are emerging as a tool to investigate protein behaviour and to relate macroscopic behaviour to the microscopic properties of the system. A wide range of application (e.g. drug discovery, protein conformational dynamics, protein mechanics, etc..) have placed Molecular dynamics as an elective methodology to simulate biological systems [70], [71].

Neurodegenerative diseases-related molecules are a topic in computational research. Fields of investigation vary from computational studies performed to understand drugs behaviour [72], [73] to molecular dynamics simulations that highlights the causes that lead to pathological hallmarks [74], [75]. Promising results have been achieved in recent molecular dynamics simulations to explain the causes leading to the aggregation of A $\beta$  peptides, indeed as reported previously, in 2.3.1. Certainly, protein aggregates are characterized by two main compounds A $\beta$ 40 and A $\beta$ 42. The first is more abundant in plaques while the latter results more toxic. Furthermore, it has been recently shown that A $\beta$ 42, differently from A $\beta$ 40, may assemble in two possible conformations, so called U-shape and S-shape. Recently, enhanced molecular dynamics simulations have compared the two above mentioned

U-Shape and S-shape architectures [76]. Results indicated the S-shape conformation as more stable when compared to the U-shape. Moreover, the architecture stability was related to hydrophobic inter-chain contacts I41-K28, A42-K28 [76]. The evidence was also confirmed by further studies highlighting the higher mechanical performance of S-shape architecture [77].

Nevertheless, amyloid stability might also be dependent by shear stress on protein surface, as indicated by *in-vitro* studies [69]. Interestingly, stable cavitation related to ultrasounds applications is responsible for generating a shear stress on the protein surface [78]. In this connection, recent, MD simulations have been performed to shed light on stable cavitation phenomena at the molecular scale [79]. Results showed that stable cavitation acts by perturbing water molecules which lately exert a shear stress on amyloid fibrils, thus driving a destabilization of the assembly.

## 3 Materials and Methods

### 3.1 *Molecular modelling*

How Molecular Modelling can be defined? Undoubtedly the word ‘Molecular’ suggests implication within molecules. While ‘Modelling’ is defined as the act of simplifying and describe a system or a process, more often in mathematical terms, with the purpose to facilitate calculation and prediction. Therefore Molecular Modelling can be termed as a set of tools to represent and simulate molecular structures and understand the properties under a given set of conditions [80]. The applications of Molecular Modelling are wide and vary from material science to biology and involves different fields of study such as physics, biology, engineering and chemistry. Since molecular systems are usually complex and made from lots of particles an analytical treatment is almost impossible hence numerical methods are necessary. For this reason, Molecular Modelling today is strictly related to computer modelling. Molecular Modelling makes use of many methods; the most accurate description of molecules is model nucleus and electron explicitly and describe the system by Schrödinger equations. However, this description, due to the high number of particles, is feasible for hundreds of atoms and even if precise, has limited application to describe a biological phenomenon. However is possible to obtain and describe accurately enough macroscopic properties of a molecules ignoring the electrons behaviour and describing only the motion of atoms nuclei, for this purpose the description of Molecular mechanics suits the needs, using force fields methods and describing the energy of the systems only in terms of nuclei position.

### 3.2 *Molecular Mechanics*

Molecular Mechanics (MM), also called force field methods, ignoring electrons motion, describes the system only as a function of nuclei position, this simplification in describing atomistic systems let to simulate systems of thousands of atoms. The rationale of this method is based on Born-Oppenheimer approximation, which assumes that electron cloud, having the electrons a much lower mass compared to the nuclei, instantaneously adjust after a changing of nuclear configuration. Therefore, a single potential energy surface (PES) is used to describe nuclear motion. Moreover, the atomic nuclei are approximated as classical particles that follows the laws of Newton [81]. A well-known limitation of the above-mentioned classical approaches is mainly related to the inability of simulating events strictly related to the description of atomic electron density clouds, such as creation on disruption of covalent bonds. The capability to develop and test parameters on a small number of

cases and transfer to applications that regards a much wider range of problems is the key attribute of a forcefield.

### 3.2.1 Potential energy function

The PES of the system in MM is described as a potential energy function (PEF) of the atomic positions. The terms of the PEF can be divided in two types of forces that pictures respectively the inter- and intra- molecular forces.

$$\mathcal{V}(r^N) = \mathcal{V}_{bond}(r^N) + \mathcal{V}_{non-bond}(r^N) \quad (1)$$

Where  $\mathcal{V}(r^n)$  is the PEF, function of the position  $r$  of the  $N$  particles in the system. On the right side of the equation the two terms represent respectively the contribution given at the energy from bond interaction such as bond stretching between two particles, angle bending between three particles and bond torsion between four particles and non-bond interaction between pairs of particles. In literature are present more complex force fields, but all have in common these four terms.

### 3.2.2 Treatment of Bond interaction

The bond interaction can be of three types:

$$\mathcal{V}_{bond}(r^N) = \sum_{bonds} \mathcal{V}_{bonds}(r^N) + \sum_{angles} \mathcal{V}_{angles}(r^N) + \sum_{torsion} \mathcal{V}_{torsion}(r^N) \quad (2)$$

Different model have been proposed to express each term of the right side.

$$\mathcal{V}_{bonds}(l) = \frac{k_i}{2} (l_i - l_{i,0})^2 \quad (3)$$

Bonds term (Figure 8 A) represent the contribution to the PEF given from two  $i,j$  atoms covalently bonded. The simplest model for the bonds stretching is Hook's law, this formulation depends only on two parameters  $k$ , called stretching constant of the bond, expressed in  $\text{kcal mol}^{-1} \text{\AA}^{-2}$ , and  $l_0$  called reference bond length or natural bond length between the two particles that interact. This kind of forces between atoms are strong and a high energy is required to deviate from the reference bond length.

$$\mathcal{V}_{angles}(\theta) = \frac{k_i}{2}(\theta_i - \theta_{i,0})^2 \quad (4)$$

The angles term (Figure 8 B) accounts the contribution to the PME due to the deviation of the angles from the valence value, valence angle is defined as the angle formed between three atoms i-j-k, where i,k are both bonded to j. Contribution from this term to the PEF has also been modelled by a Hook's law harmonic potential, this term is then characterized by other two parameters analogue to the bonds' terms, k force constant expressed in kcal mol<sup>-1</sup> deg<sup>-1</sup> and  $\theta_0$  a reference value. Compared to the energy required to stretch or compress a bond lower energy is required to distort an angle.

$$\mathcal{V}_{torsion}(\omega) = \sum_{n=0}^N \frac{V_n}{2} (1 + \cos(n\phi - \gamma)) \quad (5)$$

Torsional term (Figure 8 C) takes account of the rotation of a bond and is evaluated between four atoms, in this case the description follows a sinusoidal law, three parameters are needed to describe this term,  $V_n$  called barrier term, they accounts for the energy needed to perform a rotation, n called multiplicity give the number of minima in the function, across the variation of  $\phi$  through 360° of rotation, then the phase factor  $\gamma$  fixes where the torsion term has the minima.

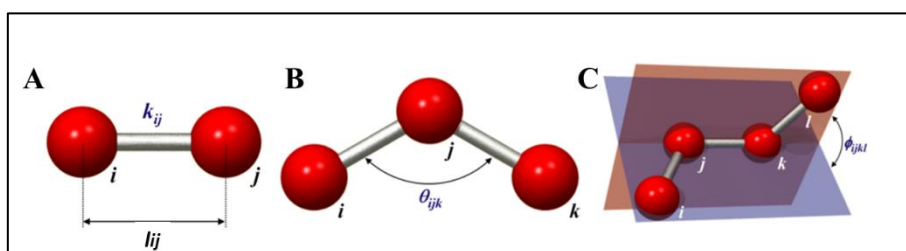


Figure 8: non-bond interaction, A stretch interaction between two atoms, B bending interaction between three atoms, C torsion interaction between four atoms

### 3.2.3 Treatment of Non-Bond interactions

Non-bond interaction is the way through which independent particles interact, this kind of potential does not depend upon any specific bound or relationship between atoms. This 'through-space' interaction is commonly expressed as a reverse power of the distance. Commonly two groups of terms are considered:

$$\mathcal{V}_{non-bond}(r^N) = \sum_{i=1}^N \sum_{j=i+1}^N \mathcal{V}_{electrostatic}(r_{ij}) + \sum_{i=1}^N \sum_{j=i+1}^N \mathcal{V}_{vanderWaals}(r_{ij}) \quad (6)$$

$$\mathcal{V}_{electrostatic}(r_{ij}) = \frac{q_i q_j}{4\pi\epsilon_0 r_{ij}} \quad (7)$$

In molecules, unequal distribution of charges arise in presence of different electronegative species, indeed less electronegative element attracts electrons not as much of more electronegative elements. A way to model this phenomenon is to distribute through the molecule different point charges. When these points are restricted to nuclei centre, they are usually referred to as partial atomic charge or net atomic charge. Then a Coulomb law describes the electrostatic interaction between two points charges  $q_i$  and  $q_j$ , and the sum of the whole interactions is given by the sum of all the electrostatic terms.

$$\mathcal{V}_{vanderWaals}(r_{ij}) = 4\epsilon_{ij} \left[ \left( \frac{\sigma_{ij}}{r_{ij}} \right)^{12} - \left( \frac{\sigma_{ij}}{r_{ij}} \right)^6 \right] \quad (8)$$

Another contribution to non-bonded terms is given by van der Waals forces, from which physical-chemical properties are partially defined. The van der Waals forces can be divided into two types repulsive, the one that act at short distances, and attractive, that act at long-range. The whole mathematical description for van der Waals interaction is given by a Lennard-Jones 12-6 function. The parameters needed to describe the interaction between two atoms are: the well depth  $\epsilon$  and the collision diameter  $\sigma$ . Van der Waals parameters are specific for each different type of particle, so a system with  $N$  different types of particles would require  $N(N-1)/2$  sets of parameters for the cross interaction between different types. A common approach is to derive the cross  $\sigma$  and  $\epsilon$  using mixing rules.

$$\sigma_{ij} = \frac{\sigma_{ii} + \sigma_{jj}}{2} \quad (9)$$

$$\epsilon_{ij} = \sqrt{\epsilon_{ii}\epsilon_{jj}}$$

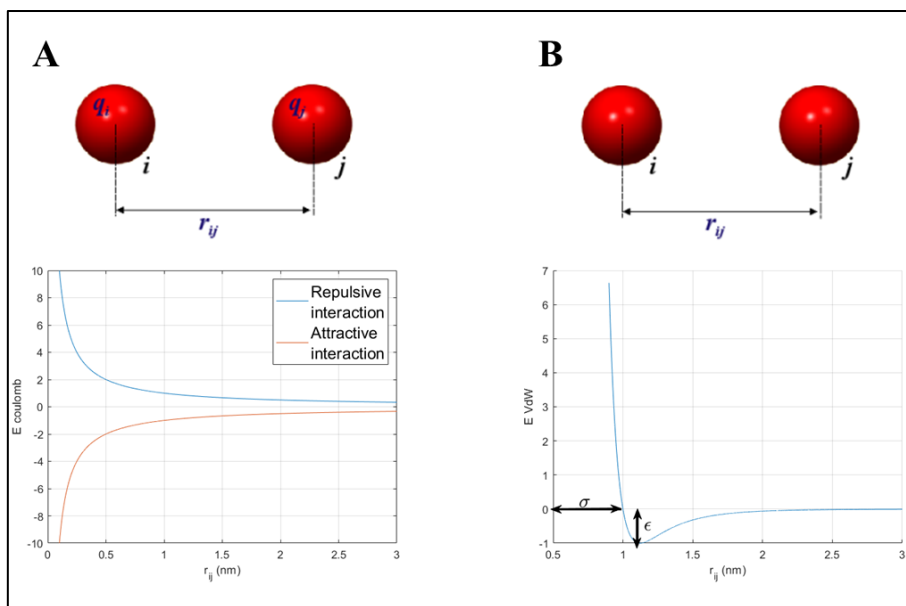


Figure 9: Non-bonded interaction, (A) Coulomb potential, (B) Van der Waals interaction.

Non bonded interaction calculations requires high computational effort, for  $N$  different particles  $N^2$  interactions are required, so different methods have been proposed to reduce that amount. The Cut-off radius method consists in ignoring the non-bonded interaction calculated for each particle over a certain cut-off, reducing the number of interactions calculated. A correct value of cut-off must be chosen to avoid instability. For this reason, an alternative method has been proposed such switch or shifted cut off, Multiple cell and particle mesh Ewald. An important requirement to correctly evaluate the contribution of non-bonded interaction is that all the particles experience forces as if they are in an infinite bulk, for this reason periodic boundary conditions are implemented in MM.

### 3.2.4 Periodic Boundary conditions

To simulate the system in a finite time, a finite number of particles are required. Usually the simulation consists in a box, of different possible shapes (cubic, truncated octahedron, hexagonal prism, Rhombic dodecahedron) with a molecule, or molecules, surrounded by water. To avoid edge effects periodic boundary conditions (PBE) are implemented, it means that the system is simulated as it is surrounded by a periodic repetition of itself in all direction. Particles in one side of the box see near them a periodic repetition of other particles of the opposite side of the box. Moreover, if a particle goes outside from the central box, another particle come from a side replica, thus the total number of particles in the main box is conserved. The error derived from this approach are usually less than the case of non-periodic boundary conditions.

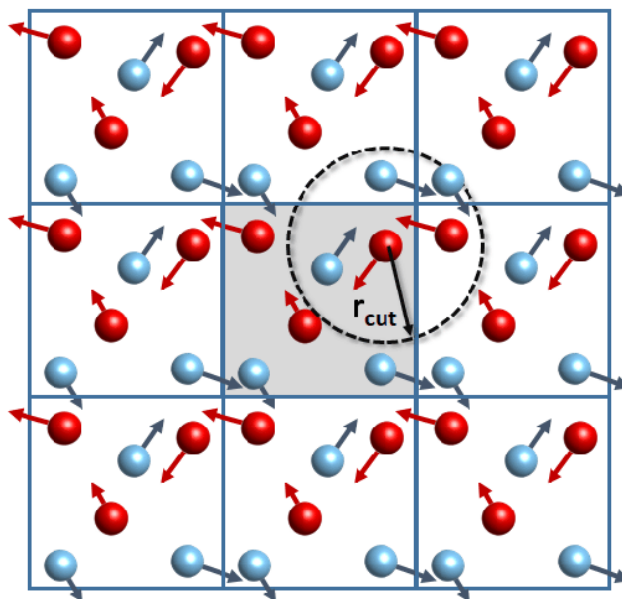


Figure 10: representation of PBC, the central box is surrounded by his replica [82]

As previously mentioned cut-off is one of the most applied method to treat the non-bonded interactions, the periodic boundary condition gives an upper limit to the cut-off value. In fact, to avoid artefacts the so-called *minimum image convention* must be consider, to impede that a particle interacts with itself. So, the cut-off radius  $R_c$  must be less than half of the minor side of the box. In case of cubic box with side vectors  $a$ ,  $b$  and  $c$ , the upper limit is:

$$R_c < \frac{1}{2} \min(|a|, |b|, |c|) \quad (10)$$

### 3.2.5 Potential Energy Minimization

The PEF that describes a system, even the easiest one is always a multidimension complicated function of the coordinates. If the system is described in terms of Cartesian coordinates, for  $N$  particles the PEF is function of  $3N$  coordinates, while in the case of internal coordinates the degrees of freedom are  $3N-6$ . Thus, to represent PEF is almost impossible and feasible only for few cases. The MM is particularly interested in the PEF minima, because these points are associated with stable arrangement of atoms. Moving away from a minimum implies configuration of higher energy level. Points where is present a minimum of energy are called *local minima*, while the lowest minimum is called *global minimum* point. To find a minimum different algorithm has been proposed in literature, all of that starts from this formal statement of the problem: considering a function  $f$ , which depends on one or more independent variables  $x_1, x_2, \dots, x_i$  find the combination of value of the variables where  $f$  reaches

a minimum value. These points are characterized by a zero value for the first derivative with respect to each variable and a positive value for the second derivative in respect to each variable:

$$\frac{\partial f}{\partial x_i} = 0; \quad \frac{\partial^2 f}{\partial x_i^2} > 0; \quad (11)$$

Methods proposed in literature can be classified into two categories, the one which use derivatives of the energy, called *derivatives methods* and the other that does not use derivative of the energy called *non-derivative methods*. Non-derivative methods account *simplex method* and *sequential univariate method*. The group of derivative methods can be divided into two sub-groups, *first order derivative methods* and *second order derivative methods*. The first group is based on the gradient, which gives information of the direction where the minimum lies. *Steepest decrescent method*, *line search in one-dimension*, *arbitrary step approach*, *conjugate gradients minimisation* belong to this group. The second group of methods use information provided from second derivatives which gives information about the curvature of the function, these values can be used to foresee where there will be a change in the direction of the function. *Newton-Raphson Method* and *Broyden-Fletcher-Goldfarb-Shann* are part of the *second order derivative methods*. No one of these methods is preferable to another, they are chose by a number of factor, such computational requirements, storage capability, the possibility of calculating the first derivative and the robustness. Energy minimization can be either used in molecular modelling as an integral part of techniques or to set a system for other kinds of calculation. In order to perform a Molecular Dynamics or a Monte Carlo simulation, energy minimization can be employed to avoid unfavourable interaction in the initial configuration.

### **3.3 Computer Simulation method: Molecular Dynamics**

Whereas MM provides the tools to describe mechanics of molecular systems and energy minimization gives a method to find an energy minimum. However these knowledges are enough to predict properties only for quite simple systems. In fact, only when all minima configurations of PES are known statistical mechanics tools can be applied to evaluate a partition function to predict thermodynamic properties of the system. However, systems of interest in this field of research are complex and the aim is to understand and predict behaviour of many particles. For this purpose, energy minimization is not enough, and other tools are needed, in order to obtain representative configuration of the system of interest and calculate thermodynamic properties in reasonable computational time. Moreover, simulation techniques can provide a tool to discover the time-

dependent behaviour, and how systems move from one configuration to another. Molecular dynamics (MD) is one of the most common simulation techniques. The rationale of MD is to solve the Newton's equations for all the particles in the system in order to obtain a trajectory of the systems in terms of positions and velocities. To understand how properties of systems can be calculated some basic concepts have to be introduced.

### 3.4 Phase space and statistical ensemble

The concept of *phase space* is fundamental in computer simulation, for a system containing  $N$  atoms, the number of values to define the state of the system are  $6N$ , (three coordinates for the position and three components of the momentum). A point in the phase space is defined by the combination of  $3N$  positions and  $3N$  momenta. An ensemble can be considered a collection of these points in the phase space. In a chemical system two main groups of macroscopic properties can be defined: static equilibrium properties (e.g. density ( $\rho$ ), Temperature ( $T$ ), Pressure ( $P$ )) and dynamic or non-equilibrium properties (e.g. diffusion, dynamic of phase change). Every point in the phase space characterizes a *Microstate* of the system, a collection of Microstates characterized by the same indistinguishable macroscopic properties is called *Macrostate*. *Statistical ensemble* is defined as a collection of points in the phase space that share the same Macrostate, in MD the principal statistical ensemble employed are:

- The Micro-canonical Ensemble (NVE) describes an isolated system, it is characterized by a fixed number of particles ( $N$ ), an assigned volume ( $V$ ) and a constant Energy.
- The Canonical Ensemble (NVT): corresponds to a closed system coupled in temperature with a thermostat, so fixed number of particles ( $N$ ), assigned volume ( $V$ ), and constant temperature ( $T$ ).
- The Isothermal-Isobaric ensemble (NPT) describes an isolated system coupled in temperature and pressure, with fixed number of particles ( $N$ ), constant temperature ( $T$ ) and pressure ( $P$ ).
- The Grand-Canonical Ensemble ( $\mu VT$ ) corresponds to an open system with fixed volume ( $V$ ), temperature ( $T$ ) and chemical potential ( $\mu$ ).

#### 3.4.1 Ensemble average, time average and ergodic hypothesis

Defined a macroscopic property of interest  $A$ , in general this value depends upon the microstate of the system. The value of  $A$  can therefore be expressed as  $A(\mathbf{p}^N, \mathbf{r}^N)$  where  $\mathbf{p}^N$  represent the momenta of all particles in the system and  $\mathbf{r}^N$  their relative positions at a given point in the phase space.

Integrating over all possible configuration of the system is possible to obtain the *ensemble average* of property A:

$$\langle A \rangle = \iint A(p^N, r^N) \rho(p^N, r^N) dp^N dr^N \quad (12)$$

Where  $\langle \rangle$  indicates ensemble average, the integral is on the  $6N$  variable and  $\rho(p^N, r^N)$  is called probability density of the ensemble, which depends upon the chosen statistical ensemble. In the case of NVT, the probability function assumes the form of the so-called Boltzmann distribution:

$$\rho(p^N, r^N) = \frac{1}{Q} \exp \left[ -\frac{H(p^N, r^N)}{k_b T} \right] \quad (13)$$

Where  $H$  is the Hamiltonian,  $k_B$  the Boltzmann's constant and  $Q$  the partition function. In case of  $N$  indistinguishable particles for the canonical ensemble is defined as:

$$Q = \frac{1}{N!} \iint dp^N dr^N \exp \left[ -\frac{H(p^N, r^N)}{k_b T} \right] \quad (14)$$

Boltzmann partition function relates microscopic thermodynamic variables that cannot be measurable with macroscopic properties. However, a correct estimation of the ensemble average is not feasible because it is extended to all the possible state of the system. To overcome this problem the ergodic hypothesis is assumed, this axiom states that ensemble averages can be replaced by time averages for long enough sampling of a certain property:

$$\langle A \rangle_{ensemble} = \langle A \rangle_{time} \quad (15)$$

For this reason, the ensemble average can be replaced by a time average.

$$\langle A \rangle_{time} = \lim_{\tau \rightarrow \infty} \frac{1}{\tau} \int_{t=0}^{\tau} A(p^N(t), r^N(t)) dt \quad (16)$$

Where  $p^N(t)$  represents instantaneous momenta of the particles in position  $r^N(t)$  at time  $t$ . By MD is possible to obtain a trajectory in terms of position and momenta for all the particles that represent the system, numerical integration over all the  $M$  steps sampled by the MD simulation gives an estimation of the average for the property of interest:

$$\langle A \rangle_{time} \approx \frac{1}{M} \sum_{i=1}^M A(p^N, r^N) \quad (17)$$

This approximation holds in the hypothesis that  $M$  is big enough to correctly sample the phase space to obtain a sufficient description of the property of interest.

### 3.4.2 Molecular Dynamics Implementation Scheme

The purpose of Molecular Dynamics (MD) simulation is to obtain a trajectory of particles in the simulated system, in terms of position and velocity, solving Newton's equation of motion. Given an initial configuration any future step of the system depends on the previous one, in this sense MD can be stated as a *deterministic* method. At each step the acceleration  $a$  of each particles  $i$ , is obtained by the derivative of the potential surface  $V$  in respect to its position  $r$ :

$$a = \frac{d^2r}{dt^2} = -\frac{1}{m} \frac{dV}{dr} \quad (18)$$

Due to the complexity of PEF, it is unfeasible to obtain an analytical solution for this differential equation, for this purpose the equations of motions are integrated using *finite difference method*. The rationale is that integration is divided in small stages, each separated from a fixed time-step  $\delta t$ . Many methods have been proposed in literature such *Verlet scheme*, *Velocity Verlet*, *Leap frog*. A crucial choice in MD simulations is the method of integration and its parameters, mainly time-step of integration is fundamental to avoid instability of the system. A trade of to regulate the value of time-step of integration, a small time-step increase computational time and the trajectory may cover a limited fraction of phase space in reasonable computational time. However too large time step can lead to instability and failure of computer simulation. A first approximation criterion would be to set the time step as ten times smaller than the faster oscillation, that in an all atom simulation is usually related to Hydrogen atoms. Shows an overall overview of a generic implementation scheme for MD simulation. Usually initial atomic positions are known from configuration obtained in literature (e.g.

from Protein Data Bank), then starting particles velocity are assigned from a Maxwell-Boltzmann distribution at a specified temperature. PEF is then built deriving bonded and non-bonded parameters from the chosen force field. Then at each step integration algorithm is applied to obtain position and velocity of next step given force of any particles from derivative of PEF in respect to atomic position. The result obtained is the trajectory of the systems in terms of atomic positions and velocity. The previous step is then repeated as many times as it has been initially set.

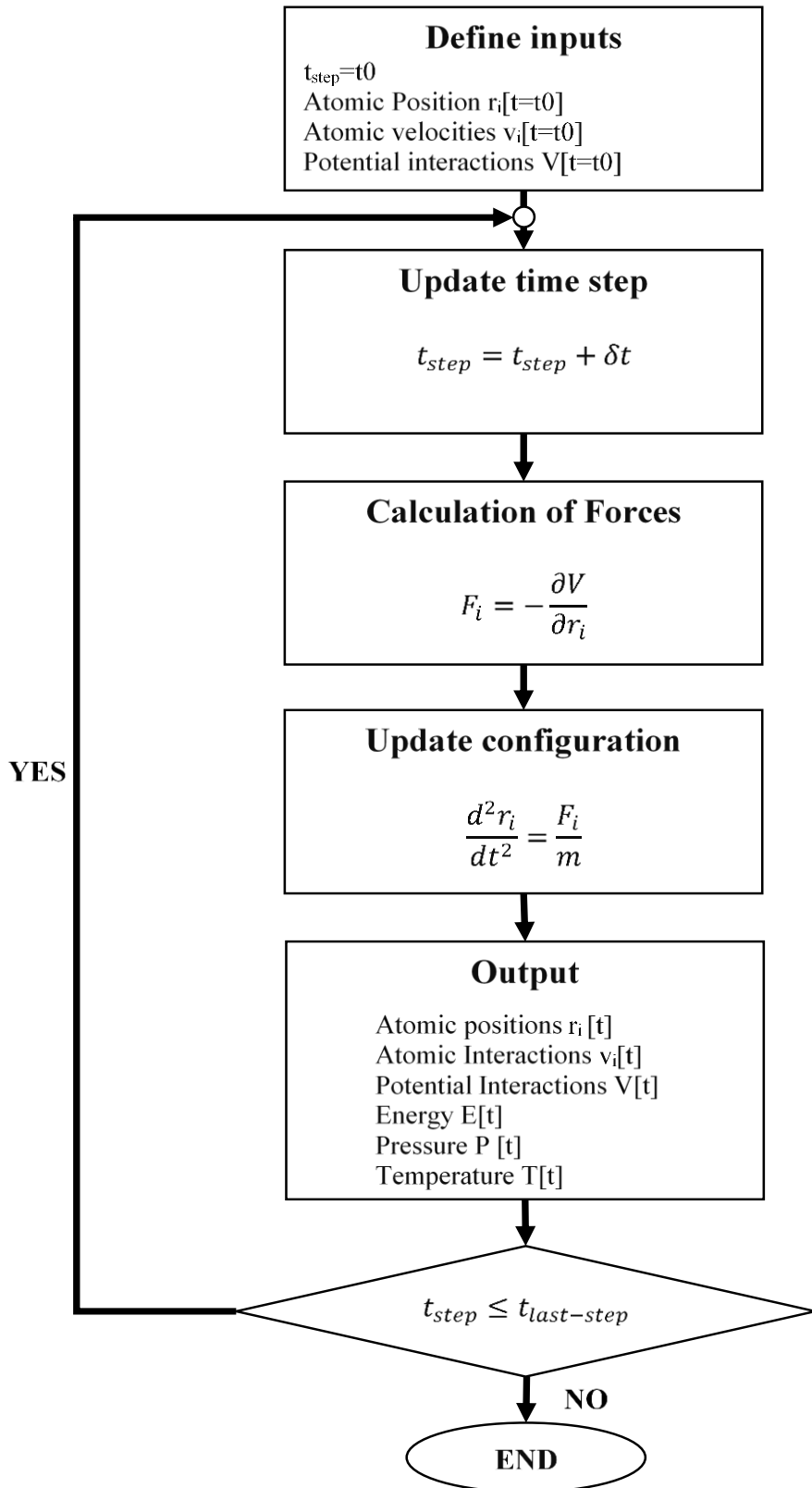


Figure 11: General scheme of Molecular Dynamics algorithm, first input parameters must be defined from an initial configuration. Then a loop on the chose number of steps is performed, for each step force are calculated as the derivative of potential energy, and then position and velocity are calculated integrating Newton's laws, the output for each step is new atomics positions, velocities, energy, pressure and temperature at the current step. The loop is repeated until total number of steps are performed.

### 3.5 Rayleigh-Plesset equation

Rayleigh-Plesset (RP) equation describes the behaviour of a spherical bubble of radius  $R(t)$ , where  $t$  is the time, in an infinite bulk of liquid, at a fixed temperature whose pressure far from bubble is  $p_\infty(t)$ . Moreover the assumption are constant liquid density  $\rho_L$  and viscosity  $\mu_L$ , it is assumed that pressure and temperature inside bubbles  $p_g(t)$  and  $T_g(t)$  are uniform. Under this assumption Rayleigh-Plesset equation states:

$$R\ddot{R} + \frac{3}{2}\dot{R}^2 = \frac{1}{\rho} \left\{ p_g(R, t) - p_\infty - p_s(t) - \frac{2\eta}{R} \right\} \quad (19)$$

Where  $p_\infty(t)$  can be decomposed in hydrostatic pressure  $p_\infty$  and  $p_s(t)$  its drift from hydrostatic pressure, and  $\eta$  is the surface tension of bulk water. The derivation of this equation can be completely done, assuming spherical symmetry, from Navier-Stokes equations [83]. For this reason, since RP equation is a continuum hydrodynamic equation, it should be not appropriate to describe nanometric and sub-nanometric bubbles vibration. However, it has been showed that if the terms describing inertia, viscosity and surface tension are correctly considered, it is possible to have a prediction, trough RP equation, of bubble dynamics behaviour in a MD simulation of nanoscale bubble cavitation. Thus its applicability to predict bubble dynamics results accurate enough also for scales [84]. Moreover, it is possible to use this equation as a tool to obtain an estimation of pressure at bubble surface,  $p_g(t) - p_\infty$ , imposing a sinusoidal behaviour of bubble radius  $R(t)$  and an external pressure  $p_s(t)$ :

$$p_g(R, t) - p_\infty = \rho \left\{ R\ddot{R} + \frac{3}{2}\dot{R}^2 \right\} + p_s(t) + \frac{2\eta}{R} \quad (20)$$

#### 3.5.1 Non-equilibrium all-atom molecular dynamics simulation of the bubble cavitation and application to dissociate amyloid fibrils

A method to simulate an all-atom MD bubble stable cavitation process was proposed in recent literature [79]. The bubble was simulated as dummy atom which changes the radius  $R$  by a modified Lennard-Jones (LJ) potential that follows an harmonic law.

$$R(t) = R_0 * \left[ 2 + \cos\left(\frac{2\pi t}{\tau} + \pi\right) \right] \quad (21)$$

where  $R_0$  is the minimum radius of the bubbles equal to 0.2 nm,  $\tau$  is the period of the sinusoid 50 ps.

$$V[r, \sigma(t)] = 4\varepsilon \left[ \left(\frac{\sigma(t)}{r}\right)^{12} - \left(\frac{\sigma(t)}{r}\right)^6 \right] \quad (22)$$

where  $\sigma(t)$  is the time dependent distance at zero potential,  $\varepsilon$  is the deep of the potential,  $r$  is the distance between the bubble and the atom on which the potential is calculated; it is also assumed that  $\sigma(t)$  is equal to  $R(t)$ . Simulation results showed that water molecules pushed back and forward, from bubble cycles of expansion and contraction, exert shear stress on fibrils thus increasing his kinetic energy.

Moreover, authors explained that the destabilization effect was not driven by bubbles hitting proteins chains. Instead, reasons for protein destabilization should be looked into bubble driven water perturbation which increases the local pressure on chains' surface. Successive cycles of compression and decompression lead the system to lose  $\beta$ -sheet structures and drive the conformation to change into isolated random coils chains.

It is worth noticing that, in experiments, bubbles radius is expected to be in the range 0.3-4  $\mu\text{m}$  and frequency range is 0.3-8 MHz. However, in MD simulations bubble radius and frequency are strictly obliged to be in the order of few nm and few GHz, respectively, due to technical reasons related to computational effort.

In this connection it can be speculated that, considering the Rayleigh-Plesset equation, bubbles radius and frequency used in simulations are enough to reproduce the same pressure effects on the protein surface as in the real situation (i.e., the experimental one). Therefore, the employed approach is meaningful to investigate the effect of ultrasound waves at molecular level.

## 4 Molecular Effects of Ultrasounds by Simulating Stable Cavitation Phenomena with Atomic Resolution

### 4.1 Introduction

Many neurodegenerative diseases have been related to aggregation of misfolded protein aggregates. Alzheimer's disease, Parkinson's disease, prion disease and other neurodegenerative illness manifest a common pathway. All these illnesses are characterized from growth of proteins aggregates, that are natively unfolded, which form fibres characterized by a  $\beta$ -sheet conformation called amyloids [85]. Pharmacological strategies have been developed to counteract these pathologies, however many of that have shown to be toxic or not effective [86], [87].

Ultrasounds techniques are widely used in medicine for their safety. Both for diagnosis, for example echography for medical imaging, and for treatment, for instance High Intensity Ultrasound (HIFU) can be used as an alternative to surgery [88], [89]. The techniques efficiency have been correlated to different physical parameter of the pulse wave: frequency, magnitude, duration of the pulses and time interval between pulses [90]. Moreover, it has been recently showed that ultrasounds can affect structure of proteins [91]. Recently has emerged from *in vitro* and *in vivo* the properties of ultrasound to disaggregates amyloid plaques [62], [66]–[68]. However, experimental measures of this phenomenon, to understand its kinetics and dynamics, are limited by the fast time scale and short length scale of the process. Furthermore, non-linearity of this process limits an analytical approach. Numerical approach, and mainly Molecular Dynamics (MD) techniques [92] allow to investigate biological systems by means of high resolution in time (nanoseconds) and length scale (nanometres).

Studies showed that disruption of amyloids aggregates driven by ultrasonic waves is related to the bubble stable cavitation phenomenon [69]. A wide number of methods have been proposed to study by MD simulation the effect of pressure waves and bubble cavitation phenomena. It has been proposed to simulate the action of shock waves, changing the momenta of waters molecules [93]. By adding, in the direction of the shock waves, a mean bias to one component of thermal velocity of selected waters molecules, contained in a restricted side of the simulation box. However, this method might be suitable for membrane only, because in this case is possible to choose a preferential direction for the ultrasonic waves, while in case of protein aggregates is preferable to avoid a directionality for the mechanical force. Another method proposed in literature is to simulate the phenomenon of bubble cavitation removing some water molecules from the system, increasing locally the temperature or applying a negative pressure on the system however this leads only to observe inertial cavitation,

while the phenomenon of stable cavitation has been related to disassembly. Literature provide a way to simulate bubble stable cavitation caused by US [79], to do that it has been created a model of stable bubble. The model consists in a low mass neutral particle that interacts with surrounding water molecules through a time dependent Lennard-Jones potential [94]. Inspired from the literature the main objective of this section has been to develop a code able to reproduce the above mentioned methodology on GROMACS [95].

## 4.2 *Materials and methods*

As first step of the work a topology for virtual bubbles was defined. Each bubble was modelled as a whole spherical space, that changes harmonically its radius size following the law:

$$R(t) = R_0 * \left[ 2 - \cos\left(\frac{2\pi n t_c}{\tau}\right) \right] \quad (23)$$

where  $\tau$  is the period of oscillation, in phase with the pressure oscillation, and the radius varies from  $R_0$  to  $3R_0$ .

Bubbles were defined as a specific atom type consisting of a dummy particle placed into the system. A time dependent Van der Waal, was set for the interaction between waters' oxygen and hydrogen atoms that follow the law:

$$V[r, \sigma(t)] = 4\epsilon \left[ \left(\frac{\sigma(t)}{r}\right)^{12} - \left(\frac{\sigma(t)}{r}\right)^6 \right] \quad (24)$$

where  $r$  is the distance between centre of mass of bubble and waters' atoms species.

The empty space generated from the repulsive part of the defined potential, mimicked the behaviour of a bubble of radius  $R(t)=\sigma(t)$ . The time dependent behaviour pushed water back and forth generating water flows. Moreover, for all other species in the system (e.g., protein atoms or ions) each bubble was considered as a single atom with the same oxygen vdW parameters, charge equal to 0 and mass equal to 16 a.m.u..

### 4.2.1 Amyloid $\beta$ U-shape model

The chosen protein model is a pentamer of Amyloid- $\beta_{17-42}$ , PDB:2BEG [34]. This model has been widely employed in literature Alzheimer's related protein aggregation investigation by MD [76], [96]. Protein residues between 1 and 16 are unstructured, so for this reason these are omitted in the protein model. While residues 18-42 are organized as a  $\beta$ -strand turn  $\beta$ -strand motif. At least two molecules are required to form two intermolecular, parallel, in-register  $\beta$ -sheets, between residues V18-S26 ( $\beta_1$ ) and I31-A40 ( $\beta_2$ ).

### 4.2.2 System Setup, Configuration and Validation

Force field chosen to model the protein is AMBER-f99SB-ILDN [97]. The protein model has been inserted in the centre of cubic box of 7.0 nm length and solvated with 8000 molecules of explicit water model TIP3P. System has been then neutralized adding chlorine ions. A number of 240 water molecules, approximately 3%, have been replaced by bubbles. Leap frog algorithm was used to integrate the equation of motion, with a time step of 0,2 fs. Electrostatic interactions were treated by particle mesh Ewald method with a short-range cut-off of 2.0 nm. Then Van der Waals interactions were treated by a plain cut-off at 1.2 nm. Potential energy minimization was performed by the steepest descend method. Two subsequent position restrained MD of 500 ps have been performed. A first equilibration in the NVT ensemble at 300 K and a second equilibration in the NPT ensemble (300K and 1 bar) were run. During the position restrained simulations bubbles radii have been fixed to  $R_0=0.3$  nm. Then, non-equilibrium molecular dynamics simulations (NEMD), in the NVT ensemble (300K), have been performed coupling the code developed to the GROMACS engine. Five 5 ns long MD replicas, starting from different initial configurations have been performed.

Results were compared with literature data concerning NEMD simulations with a similar approach on the same molecular systems [98]. Moreover, several NVT replicas were performed with "inactive" bubbles moving in the system to investigate possible result bias due to the presence of dummy atoms in the systems.

### 4.2.3 Ultrasound setup

The ultrasound code developed in this work needs two parameters to set the behaviour of ultrasound generated. The period of oscillation  $\tau$  and the radius  $R_0$ . A physical link between the behaviour of the bubbles radius and the ultrasound that generates this oscillation is described by the well-known Rayleigh-Plesset equation:

$$R\ddot{R} + \frac{3}{2}\dot{R}^2 = \frac{1}{\rho}\left\{p_g(R, t) - p_\infty - p_s(t) - \frac{2\eta}{R}\right\} \quad (25)$$

That describes the dynamics of a spherical bubble inside an infinite bulk of water, where  $R$  is the bubble radius with its first and second derivative,  $p_g(R, t)$  is the pressure inside the bubble,  $p_\infty$  is the pressure in the bulk,  $p_s(t)$  is the ultrasound pressure,  $\rho$  is the water density and  $\eta$  is the surface tension. Its applicability at molecular level has been confirmed in recent studies [84]. Chosen parameters are  $\tau=50$  ps for the period and  $R_0=0.2$  nm for the radius, in accordance to what was proposed from the reference article [84], [98].

### 4.3 Results

Results will be compared with previous literature on similar systems [84], [98].

#### 4.3.1 Conformational Analysis

A series of system snapshots are reported in Figure 12. Snapshots are extracted at different time throughout the overall MD. On the left results obtained from the procedure developed in this work, on the right results from literature. Observing Figure 12 at  $t=0$  ps in both snapshot the fibril is in his native conformation, surrounded by water molecules and bubbles (3% of the total water). After 40 periods of pressure oscillation, the fibril still maintains his  $\beta$ -hairpin-like motif. However the protein appears partially dissociated. After 5 ns the effect of water pressure drives the protein toward an unstructured conformation. At 5ns protein chains completely lost their  $\beta$ -hairpin conformation and are found disassociated into random coil isolated molecules.

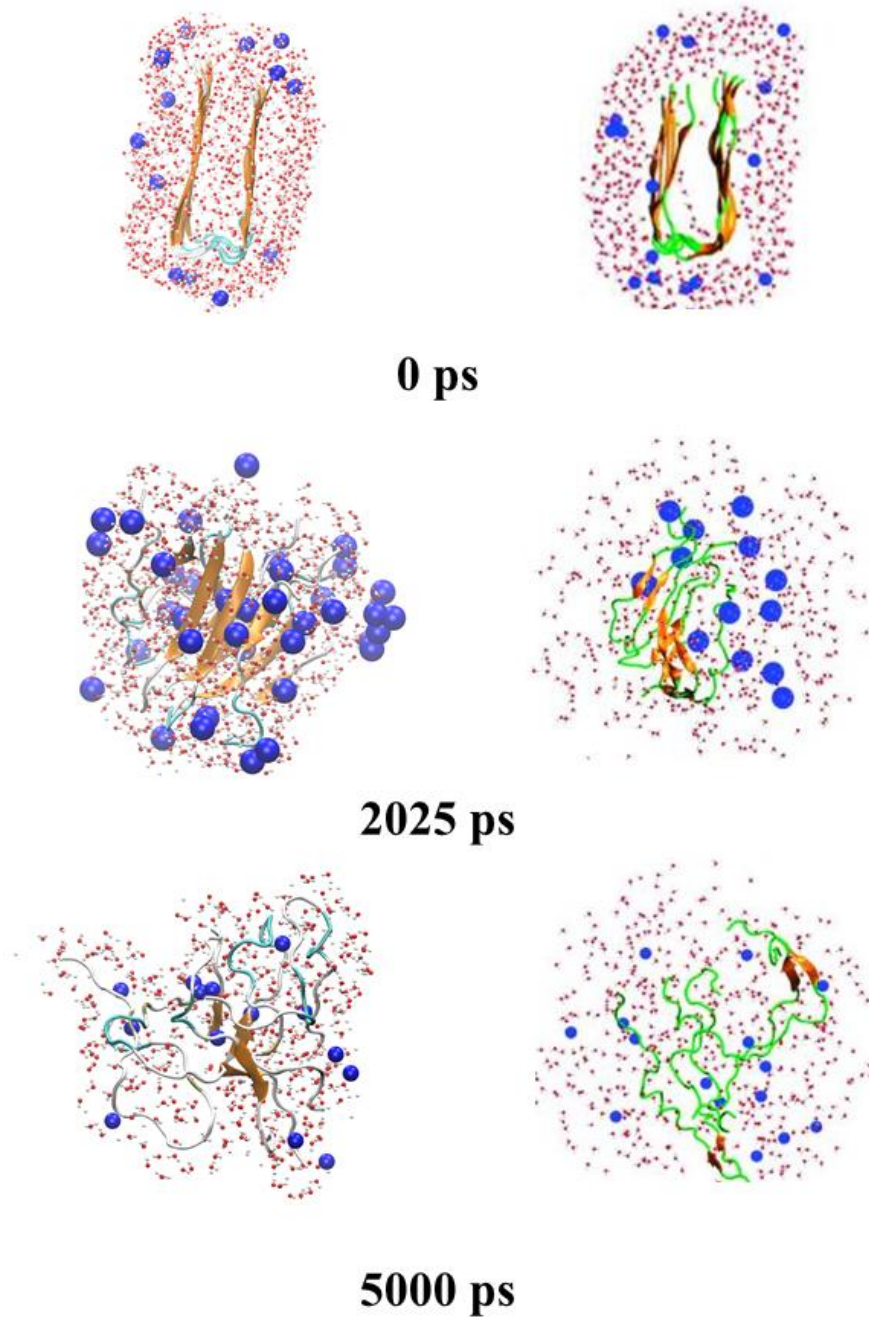


*Figure 12: MD trajectory snapshots, left (this work), right ([84], [98]). 0 ps (initial structure) with protein bubbles and water molecules. 2025 ps Bubbles reach the higher value of radius and the system start to be destabilized. 5000 ps last snapshot from both systems where the conformation is completely lost.*

The evolution of bubbles' radius throughout the overall simulation is reported in Figure 13, A. Bubble radius is quantified as the minimum distance between bubble centre of mass and the closest water molecules is reported. It is possible to observe that the measured value, in black, perfectly fits the theoretical behaviour (Figure 2A, orange). Water pushed away from bubbles expansion approaches closely to fibril as shown by the number of water molecules within 0.3 nm from any atom of the fibril

(Figure 13, B). Every time that bubbles reaches their maxima radii there is a growth water molecules approaching the protein. The drift in water molecules in time is due to defibrillation effect and consequent penetration of water into the protein assembly. The increased density of water molecules exerts locally a pressure on the fibril.

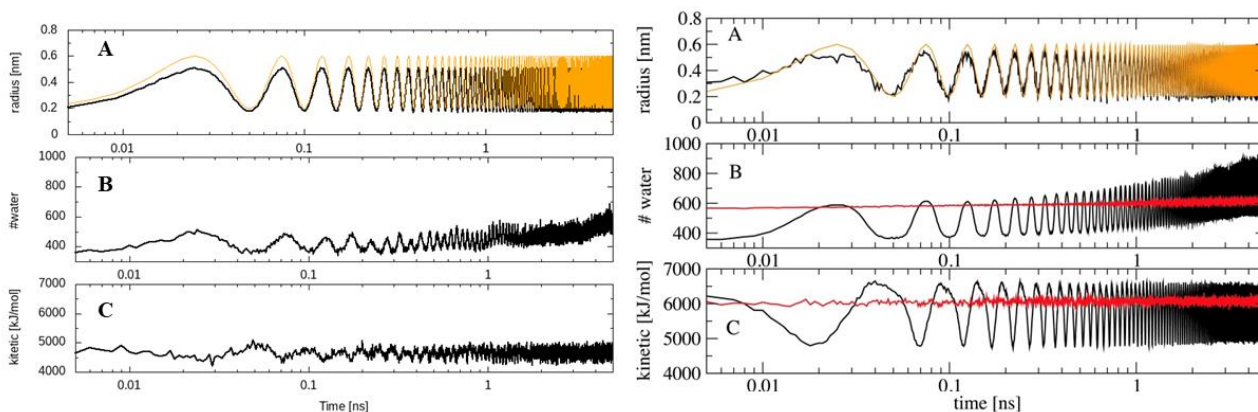


Figure 13: Analysis on bubble effect on water and fibril, results obtained from developed code, left, compared to result from literature, right. (A) the bubble radius evaluated as the minimum distance between bubble centre of mass and the centre of mass of nearest water molecules, (B) number of water molecules within a cut-off distance of 0.3 from protein, (C) fibril kinetic energy.

It is worth noticing that fibril kinetics energy, (Figure 13, C) reaches his maximum value while bubbles are contracted. The explanation of this lies in the fact that, even if water molecules exert a shear stress on the fibril pushed from bubbles, the increased pressure reduce the protein atomic motion, lowering the overall kinetic energy of protein.

Another important aspect is related to bubble vibration and fibril disassembly (Figure 14).

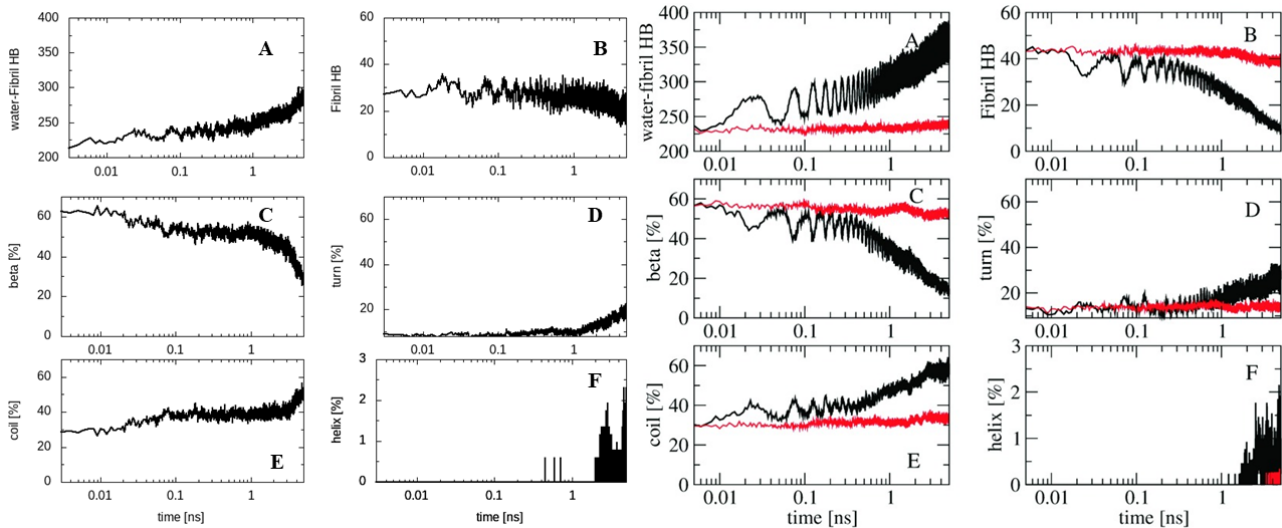


Figure 14: Destabilization of protein obtained from the developed method; left, are compared to that reported in literature, right. (A). reports time evolution of H-bond between water and fibril, (B) inter and intra chain H-bonds. From C to D evolution of secondary structure, (C)  $\beta$ , (D) turn, (E) coil and F helix.

The number of H-bond between water and protein are reported in Figure 14A. As expected, it is possible to observe that there is an “in phase” correlation with the number of water molecules previously reported. The more water molecules are close the fibril, the more H-bond are formed. The number of intra fibril H-bond is also reported (Figure 14 B). Interestingly, the reduction of inter fibril H-bond is observed together with the bubble expansion. Hence, the process of compression and decompression drives the protein to the conformational change. To observe more accurately how defibrillation process occurs, time evolution of total population of secondary structure is reported (Figure 14 C-F), evaluated by STRIDE [99] software. It is possible to remark that after the first bubble expansion,  $t=25$  ps, the percentage of  $\beta$ -structures decreases while at the same time turn and coil structure percentage increases to balance the effect. When bubbles contract, after 25 ps,  $\beta$ -structure concentration raises and protein refolds. However, subsequent cycles of contraction and expansion drive the protein toward a complete unfolding. At 5 ns the defibrillation process is concluded and is possible to observe a drastic reduction of  $\beta$ -structure, replaced by turn and coil, together with a small percentage of  $\alpha$ -helix structure.

#### 4.3.2 Structure stability analysis

Furthers analysis are performed on the system to observe the dynamics and mechanics of destabilization. To compare results a reference system that starts from the same configuration with inactive bubbles was simulated in NVT ensemble at 300 K. It is worth mentioning that bubbles behave

as water oxygen. Root mean square deviation (RMSD) for each chain, (Figure 15A), related to the initial configuration, evaluated on C-alpha is reported in order to observe the stability. It is possible to observe for the reference system that after 2 ns, values reach a plateau between 0.2 nm and 0.45 nm, with external chains showing higher fluctuations compared to internal ones. In the case of ultrasound exposure RMSD values shows a drift, that confirms the instability of the structure. Moreover effect of fluctuation are amplified for the external chains A,E, which show values of RMSD between 0.8 nm an 1.2 nm. The Root mean square fluctuation (RMSF), (Figure 15,B), shows C-alpha fluctuation averaged on each protein residues. Mean values and their min max ranges are reported for both simulations. In the case of inactive bubbles, protein residues tend to show higher fluctuation only for C-terminal tail V36-A42, related to higher solvent exposure. For the second case, under ultrasound exposure it is possible to observe higher fluctuation for residues compared to the reference system. It is possible to identify three main regions of instability at high value of fluctuation, the external tails N-terminal and C-terminal and a central region D23-I31. It is worth mentioning that in literature are reported RMSF values evaluated on Principal Components, same behaviour can be observed comparing our case to results reported [76].

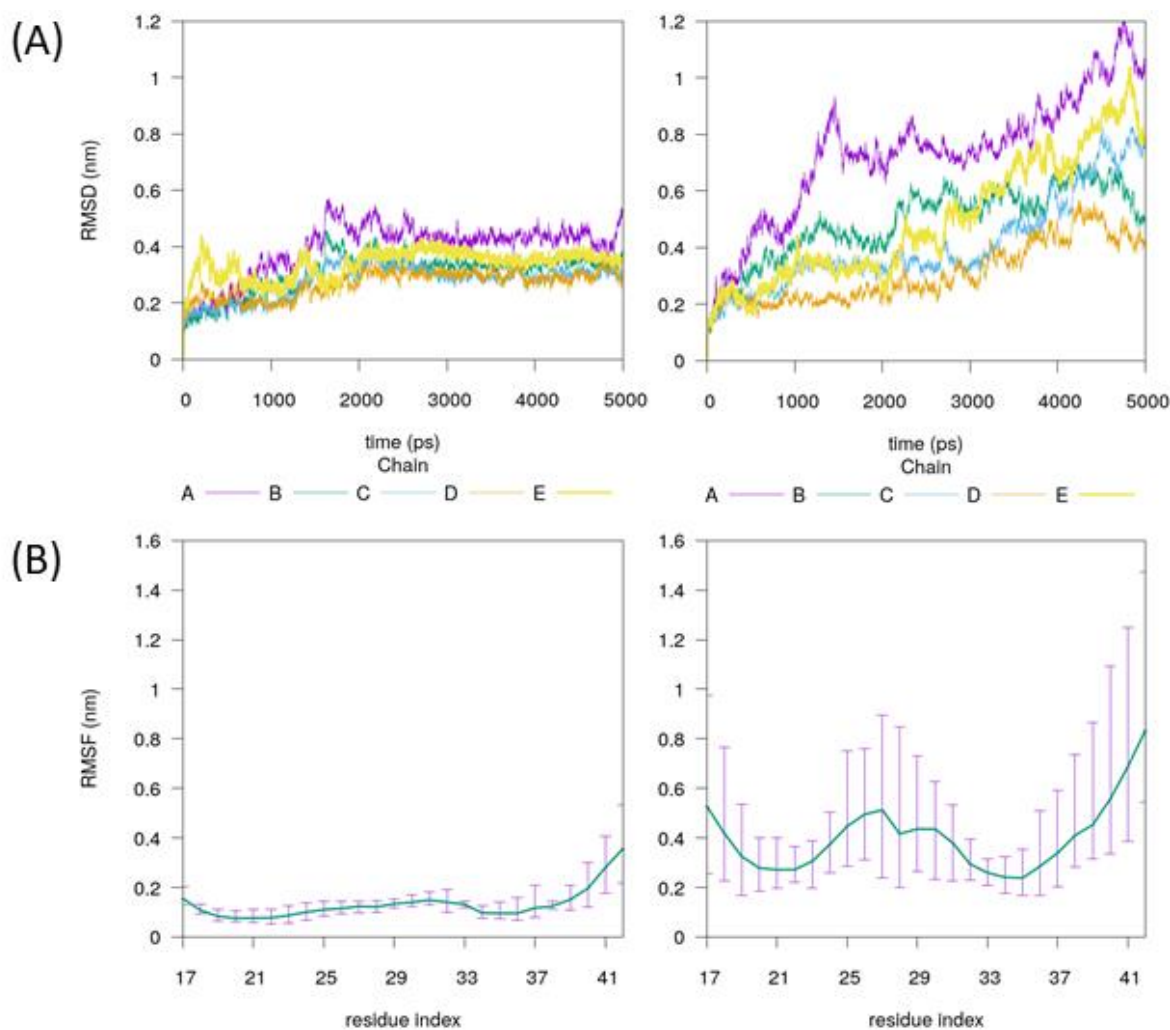


Figure 15: (A) Root mean square deviation from initial configuration evaluated on each chain for C-alpha, (B) Root mean square fluctuation averaged on residues for the whole simulation and range bar

Different stability in certain regions can be explained analysing secondary structure probability (Figure 16,A) of the two simulated systems. As done in previous literature the probability has been calculated along all chains, for windows of 1 ns, obtaining a time-residue probability. Starting condition for both models show a predominance of rigid  $\beta$ -sheets and flexible coils. Their distribution is the same for both replicas with  $\beta$ -structures situated in regions V18-D23, I31-M35 and V39-V40. However, while for the reference case the distribution is not affected by time, force exerted from the fluid flows tend to destabilize protein. It is possible to observe how external residues V39-V40 tend to lose their structure around 3 ns to 4 ns. Destabilization then occur progressively also for  $\beta$ -structures formed from residues I31-M35. At the end of process, 5 ns, the protein is completely destabilized,  $\beta$ -sheets structures have been completely lost for the C-terminal residues, also a reduced probability to find  $\beta$ -structures can be observed for N-terminal residues. Structured regions are only preserved between residues I31-M35. It is worth mentioning that results of augmented  $\beta$ -structures instability for that regions are in agreement with other computational studies [76], [100]. Moreover,

results reported for RMSF, (Figure 15), are in lines with this analysis. To deeply understand the process of destabilization, time evolution of contact probability between chain is reported, ( Figure 16, B), which provides information on residues involved into non-covalent interactions responsible for protein assembly and disassembly. Contact probability is calculated on windows of 1 ns as an average over all pair of chains that are in contact (chains A-B, B-C, C-D, D-D). Both initial configurations show high values of contact probability close so 1, as the case of secondary structure probability first system is stable for all the simulation, it is possible to see a loss of contact only for C-terminal residue A42, due to the higher water exposure and the unstructured behaviour of this residue. Contact probability evaluated in presence of ultrasounds shows a progressive loss of contact, between 2 ns and 3 ns, in particular in the area V39-V40. The breach precedes throughout the simulation resulting in a chain-chain separation in roughly 3 ns. Together, the unstructured region (residue range V24-A30) lowers the contact probability and undergoes through a progressive disruption of inner secondary structures. Results of contact probability are in accordance with recent studies on stability of U-shape model, that showed a reduced stability due to residue fluctuation in above highlighted regions [24].

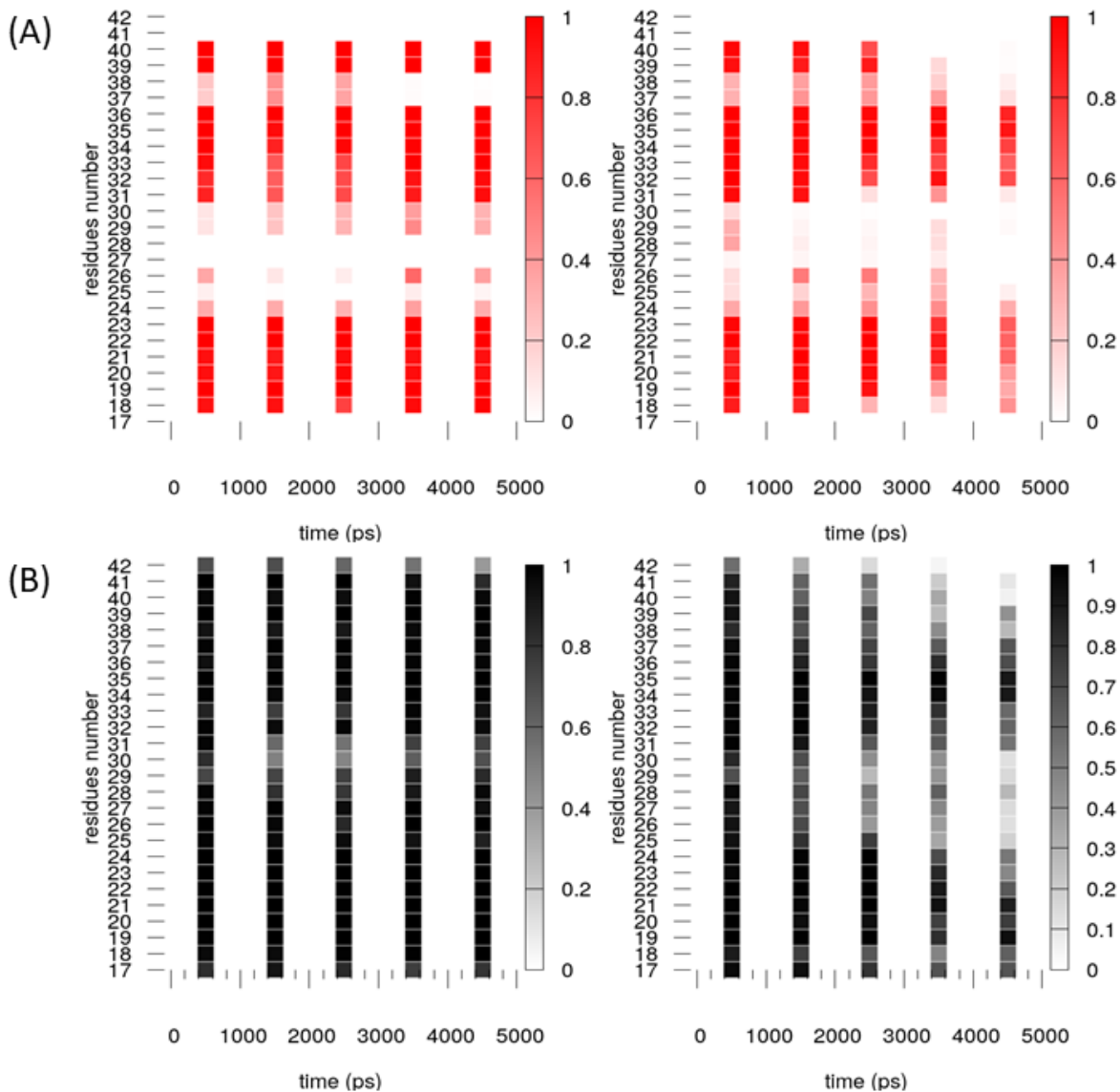


Figure 16: On the left the reference system, on the right the system exposed to ultrasound. (A) residue secondary structure probability calculated over 5 chains (A-E) every 1 ns. (B) contact probability averaged on each chain in contact (A-B, B-C, C-D, D-E).

## 4.4 Discussion

In this Chapter the “ultrasound” code developed in this work has been employed to destabilize a U-shape amyloid fibril. Results have been compared with a very similar approach applied on the same system, reported in earlier literature [84], [98]. The close agreement with recent literature provided a strong proof concerning the validity of the present code. In particular, behaviour of bubbles’ radius perfectly fits trend reported in literature. This analysis is confirmed from successive results that shows the numbers of water molecules that approach the fibril. Kinetic energy trend fits in terms of variation,

being in counter phase to bubble vibration. Common trends were also found for destabilization analysis, e.g., H-bond and secondary structure population.

It is worth mentioning that in real case bubble cavitation radius and typical frequency are expected to vary in the range 0.5-4  $\mu\text{m}$  and 0.3-8 MHz, respectively [101]. However, to obtain result for an all atom MD simulation, in reasonable time, higher frequency and lower radius must be chosen. Moreover, it has been proposed that the mechanism of defibrillation driven from shear stress exerted from water should be the same [84], [98]. Results obtained have been then analysed to determine mechanical and dynamical behaviour of destabilization. It is possible to observe from RMSD analysis higher fluctuation for the system exposed to ultrasounds. From RMSF analysis is possible to highlight more instability for less structured residues. It is worth to mention that recent Molecular Dynamics studies performing functional mode analysis on U-shape model of Amyloid- $\beta_{17-42}$  (reference material), showed an analogue behaviour, in terms of RMSF, as the case of ultrasound exposure, this fashion can be correlated to the fact that mechanical shear stress exerted by water molecules let the protein move following his normal mode of vibration. Time evolution of secondary structures and contact probability provides a description of fibril disaggregation. Indeed, fibril start to lose contact and then his secondary structure from residues less structured like regions I41-A42 and D23-I31. These defects then propagate reducing stability of closer residues driving protein defibrillation.

In conclusion this Chapter has highlighted the “ultrasound” code developed in this work as useful to: 1) investigate the molecular effects of ultrasounds applied to a biological system, and 2) to investigate amyloid fibril stability acting a destabilizing source for the fibril.

## 5 Ultrasonic waves effect on $\beta$ -amyloids conformational dynamics by non-equilibrium molecular dynamics simulation

### 5.1 Introduction

Alzheimer is a neurodegenerative disease, characterized by an abnormal aggregation of  $\beta$  amyloid protein into plaque in the brain[15]. Primary aminoacidic sequence of  $\beta$  amyloid has 42 residues. Most frequently the principal components in amyloid plaques are  $A\beta$  peptides 1-40 ( $A\beta$ 40) and 1-42 ( $A\beta$ 42). While  $A\beta$ 40 has been found to be most abundant component in plaques,  $A\beta$ 42 showed higher toxicity forming fibrils more rapidly. Even if these two peptides differ only for two residues, they show different accessible conformations. While  $A\beta$ 40 aggregates form only a U-shape motif, characterized by two central  $\beta$ -strands,  $A\beta$ 42 arrange also into an S-shape motif where three  $\beta$ -strands are connected by two coils regions [102]. Recently enhanced molecular dynamics simulations were performed to compare structural stability for the U and S-shape conformations. Results obtained performing a Replica exchange molecular dynamics simulation support for the stability of S-shape model. On the other hand U-shape model showed a more disordered conformation and a reduced stability [76]. It was suggested that hydrophobic contacts characterizing U-shape architecture tend to increase stability of the protein. Moreover, further analysis of Steered Molecular dynamic simulation was performed to investigate mechanical properties related to different architecture showed from  $A\beta$ 42. Supplementary confirms of enhanced mechanical properties for S-shape model, supports the hypothesis that stability of protein aggregates can be influenced by conformation architecture of the protein [77]. Results on S-shape model of  $A\beta$ 42, configure this conformation as an elective target to develop strategies for modulate aggregation of amyloid fibrils. It is worth mentioning that to compare U-shape and S-shape models, some residues for the S-shape conformation (E11-K16) were removed in respect to the original structure model. This chose was done to compare the protein model to U-shape. Indeed, residues between E11 to K16 are not structured and commonly omitted in protein model. However, S-shape residues in that region results involved in a  $\beta$ -strands conformation. It has been then proposed from authors that neglecting that residues can affect the structure stability [76].

As discussed in previous chapter, ultrasounds has been proposed as a non-pharmacological strategies to disaggregates amyloid plaques [62], [66]–[68]. Different computational method to perform ultrasound simulation at molecular level has been proposed [79]. The purpose of previous chapter has been to validate a code inspired from the recent literature, to perform an all atom molecular dynamics simulation of bubble stable cavitation. Method has been then tested on the U-shape model of  $A\beta$ 42.

However, as is emerged from literature S-shape model of A $\beta$ 42 has showed an enhanced stability compared to U-shape conformation. Aim of this chapter is to evaluate the stability of S-shape model of A $\beta$ 42 under ultrasound excitation. Results will provide an overall view to destabilization of A $\beta$ 42 protein driven by ultrasound. Moreover, recently an all residue model of A $\beta$ 42 has been published and a protein model has been released in Protein data Bank (PDB). For this reason, two protein model for S-shape A $\beta$ 42 have been investigated, and in particular A $\beta$ <sub>11-42</sub> and A $\beta$ <sub>11-42</sub>. A first analysis of the stability of the two models will be performed, then a comparison between the two models will be performed to highlight the effects on stability of N-terminal residues. Results will be summarized in conclusion to present an overall view of destabilization of A $\beta$ 42 protein conformations driven by ultrasound.

## **5.2 Materials and methods**

### **5.2.1 Amyloid $\beta$ S-shape models**

Two protein models for the A $\beta$ 42 S-shape protein were considered: the S-shape A $\beta$ <sub>11-42</sub> (PDB ID:2MXU [36]), (Figure 17: Protein models, (A) the S-shape A $\beta$ <sub>11-42</sub> (PDB ID:2MXU [36], (B) S-shape A $\beta$ <sub>1-42</sub> (PDB ID:5OQV [37])Figure 17, A), and the recently resolved model of A $\beta$ 42, the S-shape A $\beta$ <sub>1-42</sub> (PDB ID:5OQV [37]), (Figure 17: Protein models, (A) the S-shape A $\beta$ <sub>11-42</sub> (PDB ID:2MXU [36], (B) S-shape A $\beta$ <sub>1-42</sub> (PDB ID:5OQV [37])Figure 17, B). 2MXU model consist in a protein fibril where chains accounts residues from E11 to A42. 5OQV model consist in a fibril of parallel where all the residues of A $\beta$ 42 were considered. A pentamer was extracted both from 2MXU and 5OQV PDB models. 2MXU model show three extended  $\beta$ -strand connected by two loop regions. First  $\beta$ -strand is the N-terminal ( $\beta$ 1) V12-V18, then the central strand ( $\beta$ 2) V24-G33 and the latter C-terminal ( $\beta$ 3) V36-V40. While 5OQV is slightly different, always three regions involved into  $\beta$ -strand are present, however secondary structure are formed into the N-terminal ( $\beta$ 1) tail and involves residues between E3-E22, in the central  $\beta$ -strand ( $\beta$ 2) formed from residues K28-M35 and at C-terminal strand ( $\beta$ 3) compose by residues V40-I41. In this section each structure will be referred through its PDB ID.

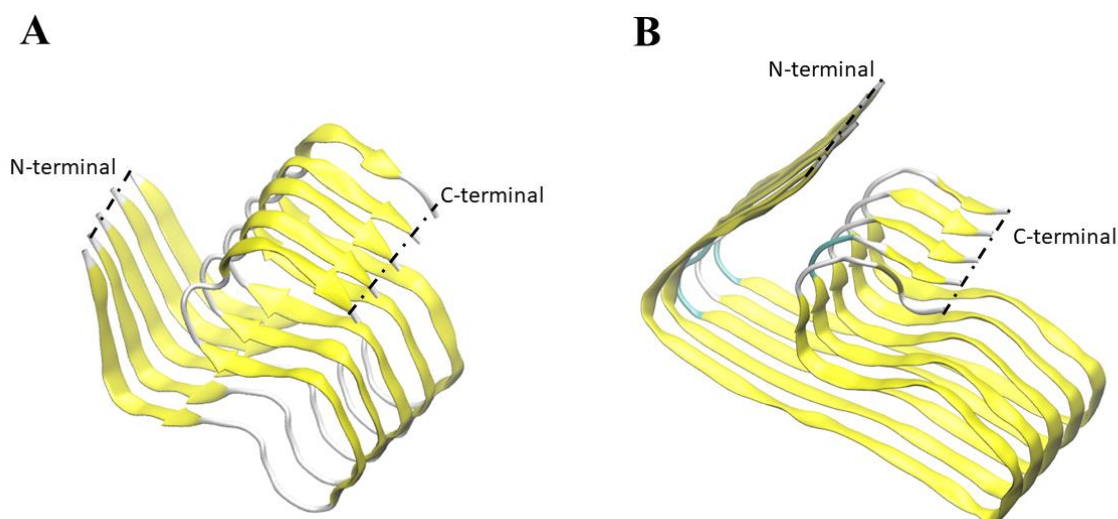


Figure 17: Protein models, (A) the S-shape Aβ<sub>11-42</sub> (PDB ID:2MXU [36], (B) S-shape Aβ<sub>1-42</sub> (PDB ID:5OQV [37])

### 5.2.2 System setup and Configuration

Both protein have been modelled through force field AMBER-f99SB-ILDN [97]. For each protein model the same procedure was followed, in order to set up two different simulations. The protein model was inserted in the centre of cubic box of 8.0 nm length and solvated with around 15000 molecules of explicit water model TIP3P. Neutralization of both systems was obtained adding a concentration 0.15 Mol of chlorine and sodium atomic types. As done in previous section approximately 3% of waters molecules have been replaced from bubble atomic type. Leap frog algorithm was used to integrate the equation of motion, with a time step of 0,2 fs. Electrostatic interactions were calculated using particle mesh Ewald method with a cut-off of 1 nm. Then Van der Waals interaction were treated by a switch cut-off that from 0.9 to 1 nm. A first minimization procedure was performed on the systems using the step decrescent method. Restraints have been applied only to the protein to perform two sequential equilibrations of the systems. Firstly, an equilibration of 250 ns in NVT ensemble at 300 K and secondly an equilibration of 500 ns in NPT ensemble (300 K and 1 bar) were run. Temperature and pressure were maintained at equilibrium through v-rescale algorithm [98]. During position restraints bubbles radii have been fixed to  $R_0=0.3$  nm. After the preliminary steps, the ultrasound simulation was performed. GROMACS engine was coupled to the code developed in the previous chapter to perform non-equilibrium molecular dynamics simulations (NEMD) in an NVT ensemble (300K).

For each system two replicas were run; length of simulation was not decided *a priori*. Runs were concluded when disaggregation of protein *has* observed.

Results from ultrasound simulations have been compared to a reference system. As done in previous chapter an NVT replica of 100 ns were performed with “inactive” bubbles. Then trajectories were extracted from NVT replicas to be comparable in length, depending on destabilization time observed for 2MXU and 5OQV systems respectively. To compare results a reference system that starts from the same configuration with inactive bubbles was simulated in NVT ensemble at 300 K.

### 5.2.3 Order parameter analysis

As done in previous literature [76], [77], [103], an order Parameter (orderP) was implemented in order to study structural stability of fibril and alignment between protein chains. General formulation for the order parameter was:

$$ordP = \frac{1}{N} \sum_{r=\min(resindex)}^{42} \frac{\langle v_r, x \rangle}{||v_r|| \cdot ||x||} = \frac{1}{N} \sum_{r=\min(resindex)}^{42} \cos\alpha \quad (26)$$

Where  $v_r$  is a corresponding vector between  $C_\alpha$ -atoms of correspondent residues in chain A and E,  $r$  is the residue index and  $x$  are the fibril axis. Value of orderP close to 1, correspond to a structure where chains maintain an alignment to initial structures. Value above 1 reveals that overall structure order decrease.

## 5.3 Results

### 5.3.1 Analysis of structure stability for 2MXU

Time evolution of order parameter evaluated on the fibril has been reported, and a series of system snapshots were extracted from the trajectory at different time steps Figure 18. Through all the simulation is possible to observe a decrease of the OrderP. Reduction in OrderP reflects a lowered order for the fibril. Snapshots, at different time step, reporting fibril structure confirms that for low value of order parameter fibril results less structured. It must be said that order parameter loses its meaning for angles higher than  $35^\circ$ ,  $OrderP < 0.6$ , however it is possible to observe that reduction in order parameters reflect in unstructured configuration.

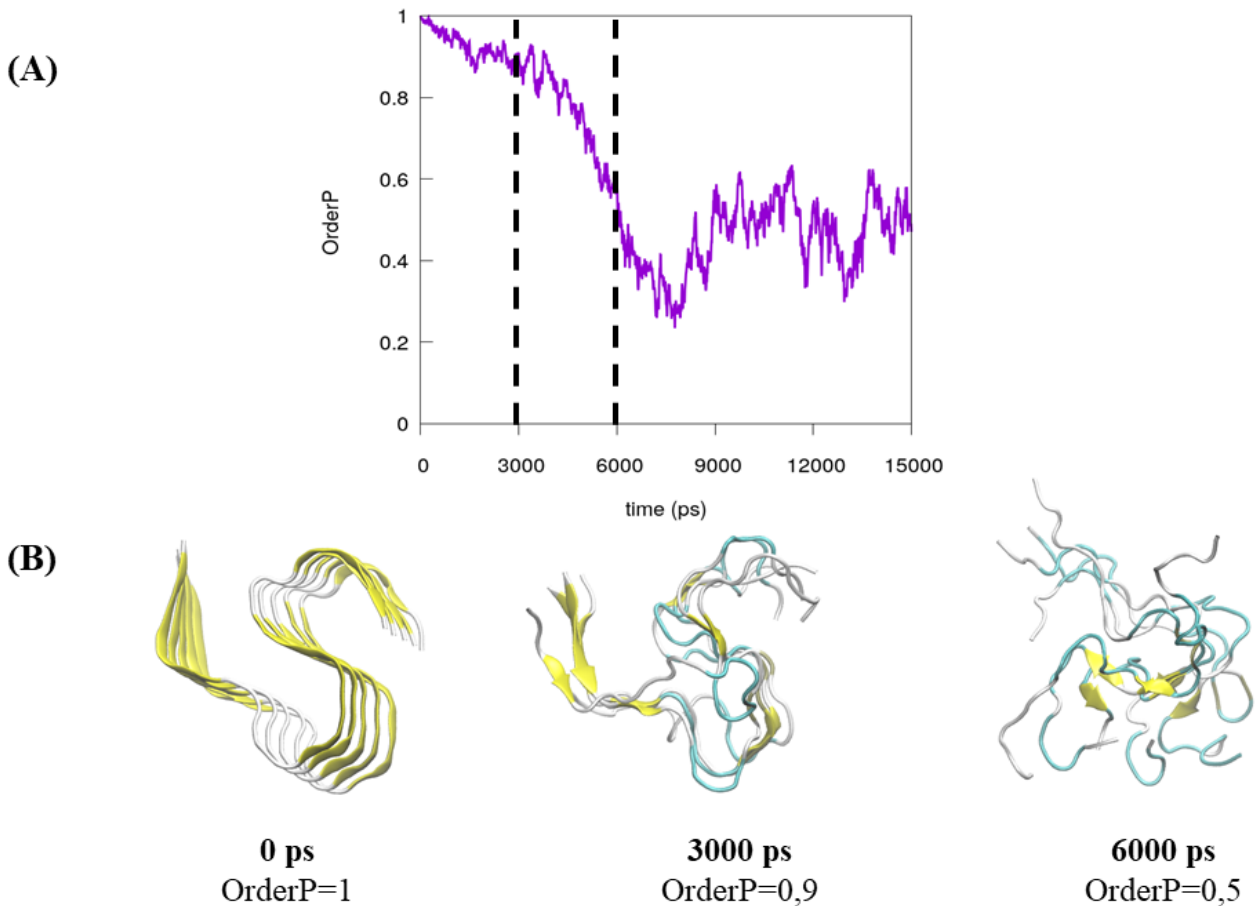


Figure 18: (A) time evolution of the order Parameter for the 2MXU protein under ultrasound exposure, (B) snapshot at different time step of the system. 0 ps the system is highly ordered showing the typical S-shape conformation, 3000 ps system start to lose order many secondary structure are lost and order parameters start to decrease, 6000 ps system is completely disordered, almost all secondary structure are vanished. For the seek of clarity protein snapshot have been coloured on the base of the secondary structure,  $\beta$ -sheet (yellow), turn (blue) and coil (white).

Root mean square deviation (RMSD) for each chain, (Figure 15A), related to the initial configuration, evaluated on C-alpha is reported in order to observe the protein stability. Stability of the reference system is confirmed by RMSD analysis. It possible to observe that RMSD values reach a plateau around value of 0.2 nm at 1 ns, lower fluctuations vanish after 6 ns. In the case of ultrasound exposure simulation, RMSD values show a drift, that confirms the instability of the structure. Studying the behaviour of RMSD for each chain is possible to observe that external chains A,E, showing higher values of fluctuation. This observation can be explained due to an higher exposed to water shear action, and a related higher tendency to disaggregates. The Root mean square fluctuation (RMSF), (Figure 15B), shows C-alpha fluctuation averaged on each protein residues. Mean values and their min max ranges are reported for both simulations. In the case of inactive bubbles, an almost flat behaviour of fluctuation is observed, data of RMSF agree to RMSD, confirming the stability of the structure. Instability which emerges from the RMSD of ultrasound case, results also in the evaluation

of RMSD . In fact, it is possible to observe higher fluctuations for residues compared to the reference system. It is possible to identify three main regions of instability at high value of fluctuation, the external tails N-terminal and C-terminal and a central region D23-I31.

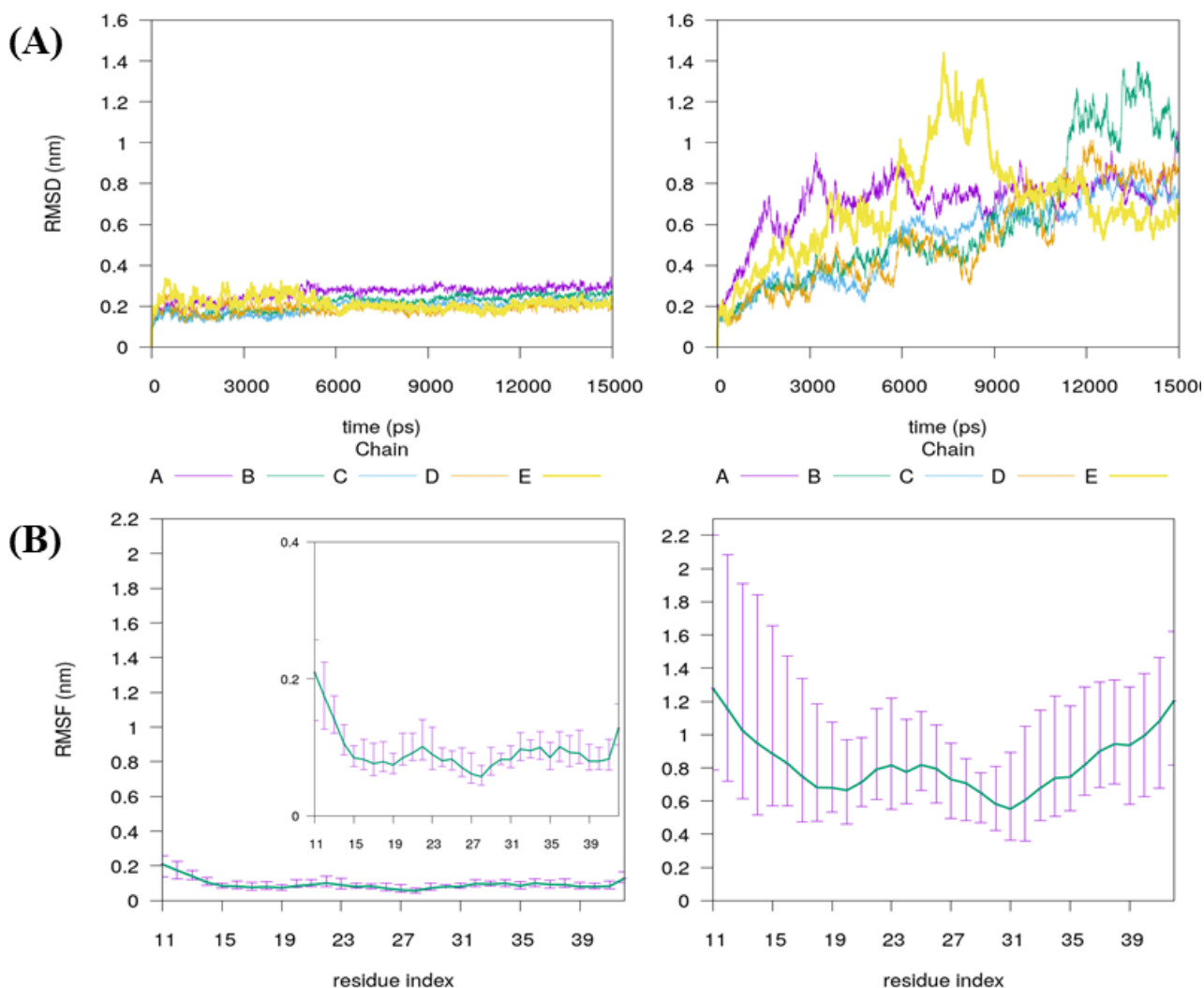


Figure 19: 2MXU model, (A) Root mean square deviation from initial configuration evaluated on each chain for C-alpha, (B) Root mean square fluctuation averaged on residues for the whole simulation and range (min max) bar, and for the reference case same data are plotted with a different scale

Dissimilar stability in certain regions can be elucidated by analysing the secondary structure probability (Figure 16,A) plot concerning the two simulated systems. As done in previous literature [104]–[106] the probability has been calculated along all chains, for windows of 1 ns, obtaining a time-dependent probability per residue. Starting condition for both models show a predominance of rigid  $\beta$ -sheets and flexible coils. Their distribution is the same for both replicas with  $\beta$ -structures situated in V12-V18, V24-G33 and V36-V40. It is possible to observe around 1 ns to 2 ns for the reference case that  $\beta$ -sheets conformation is lost at residues V36-G38, G33, V24, however stability

of the structure is maintained. In fact, other  $\beta$ -structure lead to a stable behaviour for all the simulation period, confirming the intrinsic stability of the structure. In the second case, shear stress exerted by water molecules destabilize secondary structures leading to a complete disaggregation around 6 ns. C-terminal region  $\beta$ -sheets probability vanish between 3 ns and 4 ns. Then, around 5 ns to 6 ns N-terminal  $\beta$ -strands formed from residues V12-V18 is lose. The most stable area result to be the  $\beta$ 2 central strand, that is lost after 6 ns. Results obtained from ultrasound simulations appear to be in contrast to previous computational studies, indeed C-terminals residues resulted more stable than N-terminals, while from this simulation an opposite behaviour emerges, however it is worth mentioning that authors did not consider last residues of 2MXU model, suggesting that this chose would have affect 2MXU stability [76]. Moreover, results reported for RMSF, (Figure 15), are in lines with this analysis. To deeper understand the process of destabilization, time evolution of contact probability between chain is reported (Figure 16B), in order to understand which residues are involved into non-covalent interaction and where the destabilization process starts. Contact probability is calculated on windows of 1 ns as an average over all pair of chains that are in contact (chains A-B, B-C, C-D, D-D). Both initial configurations show high values of contact probability close to 1, as in the case of calculation of secondary structure probability, reference system is stable for all the simulation, while US systems shows a progressive loss of contact between chains. Unstructured residues characterized by an higher fluctuation show higher tendency to lose contact. Then, in results to the increased fluctuation caused by ultrasound exposure, loss of contact propagate from residues less structured to close structured residues. This phenomenon precedes loss of secondary structure in regions close to coils.

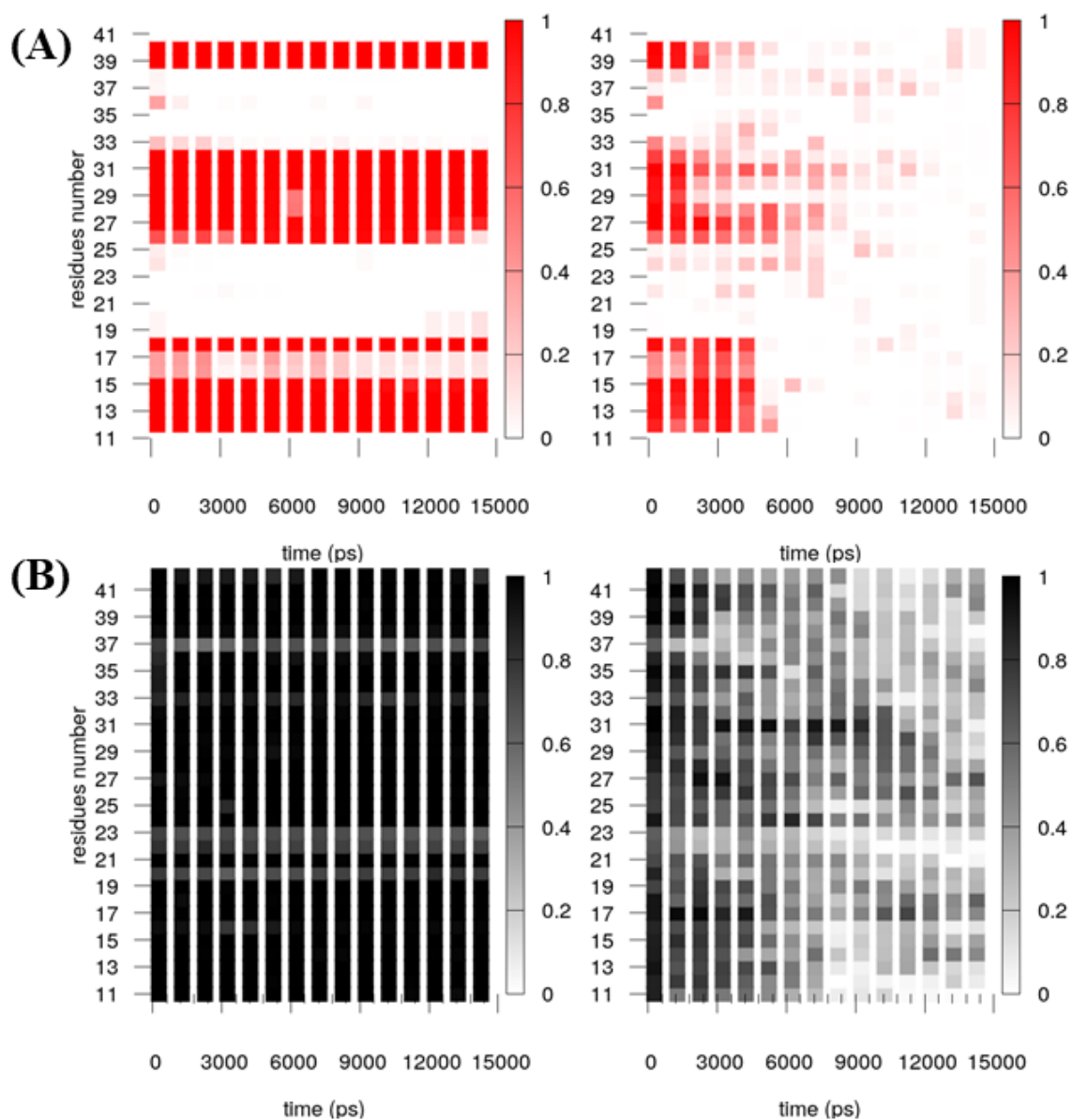


Figure 20: On the left the reference system, on the right the system exposed to ultrasound for 2MXU model. (A) residue secondary structure probability calculated over 5 chains (A-E) every 1 ns. (B) contact probability averaged on each chain in contact (A-B, B-C, C-D, D-E).

### 5.3.2 Analysis of structure stability for 5OQV

Analogue analyses of the previous section were performed to elucidate dynamics and mechanics of destabilization for 5OQV. Time evolution of order parameter evaluated on the fibril has been reported, and a series of system snapshots were extracted from the trajectory at different time steps in Figure 21. Order parameters showed a tendency to decrease through all the simulation time. A momentary inversion in tendency can be observed around 10 ps to 15 ps. This behaviour can be linked to a tendency of the fibril to temporally refold. In fact, it is possible to observe that around 15 ns the protein shows a fibril structure (Figure 21B). However, at 45 ns protein lose almost his characteristic shape preserving few  $\beta$ -structures (Figure 21B). After 75 ns protein results completely unfolded.

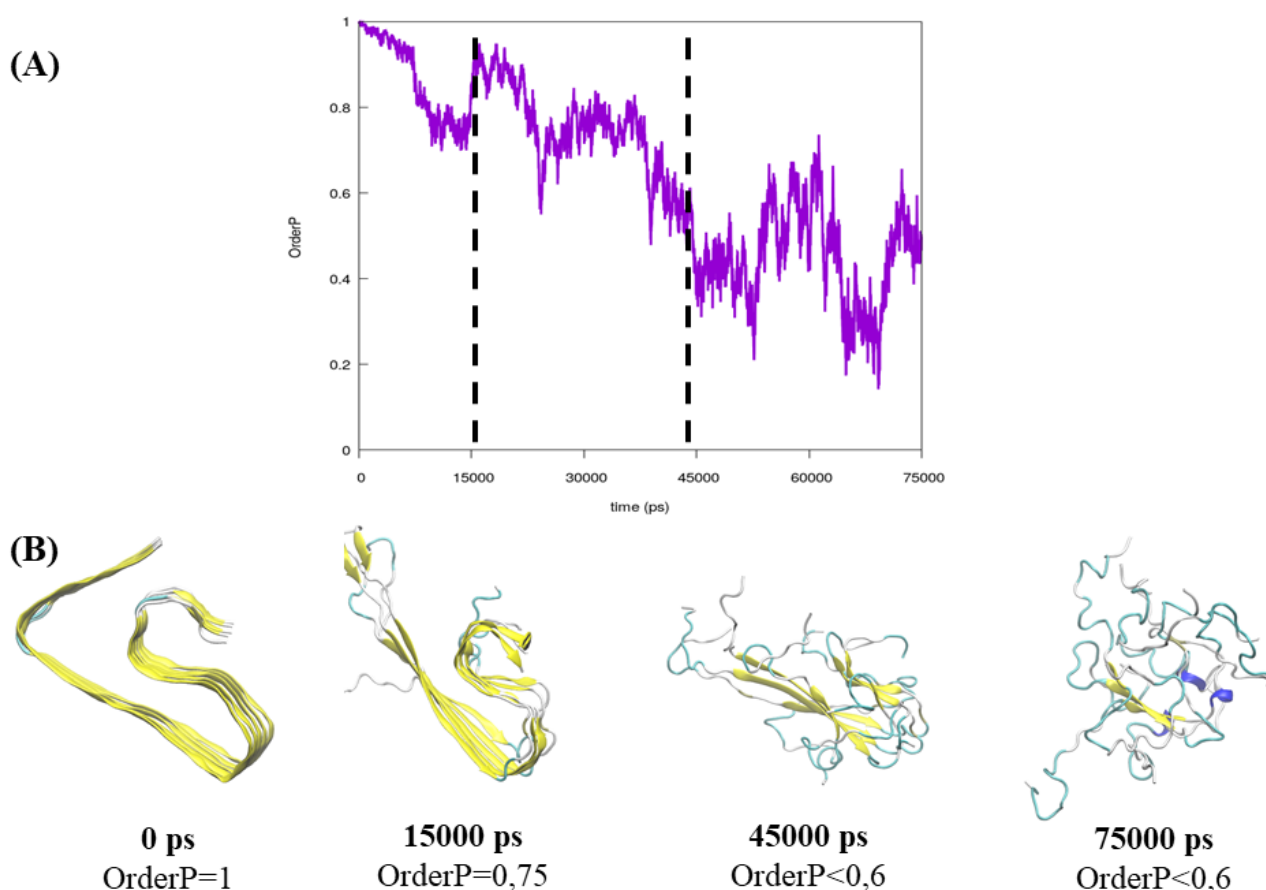


Figure 21: (A) time evolution of the order Parameter for the 5OQV protein under ultrasound exposure, (B) snapshot at different time step of the system. 0 ps the system is highly ordered showing the typical S-shape conformation, 15000 ps, order parameters shows a downhill, this behaviour can be related to the fact that protein potential energy function present a local minimum, 45000 ps system is highly disordered, only  $\beta$ 2 region is conserved, 75000 ps system is completely unstructured. For the sake of clarity protein snapshot have been coloured on the base of the secondary structure,  $\beta$ -sheet (yellow), turn (blue) and coil (white),  $\alpha$ -helix in blue.

Root mean square deviation (RMSD) for each chain, (Figure 22,A), related to the initial configuration, evaluated on C-alpha is reported in order to observe the stability. Stability of the reference system is confirmed from RMSD behaviour; indeed, it is possible to observe that values reach a plateau around 0.2 nm. In case of ultrasound simulation, RMSD values show a drift though all the trajectory, that confirms the instability of the structure. RMSD of chain A, in respect to other chains, shows higher values. This behaviour agrees with previous simulation, where external chains, due to the higher surface exposed to the shear stress exerted from water, tend to be destabilized before internal chains. Root mean square fluctuation (RMSF), (Figure 22,B), shows C-alpha fluctuation averaged on each protein residues. Mean values and their min max ranges are reported for both simulations. Data of RMSF confirms the stability of the reference system, in accord to RMSD values. Indeed nonappreciable fluctuation is observed. For the second case, ultrasound exposure drives residues fluctuate more compared to the reference case. It is possible to observe that external tails fluctuate more compared the protein core. N-terminal tail showed higher value of fluctuation, moreover a peak can observe between residues A21-S26.

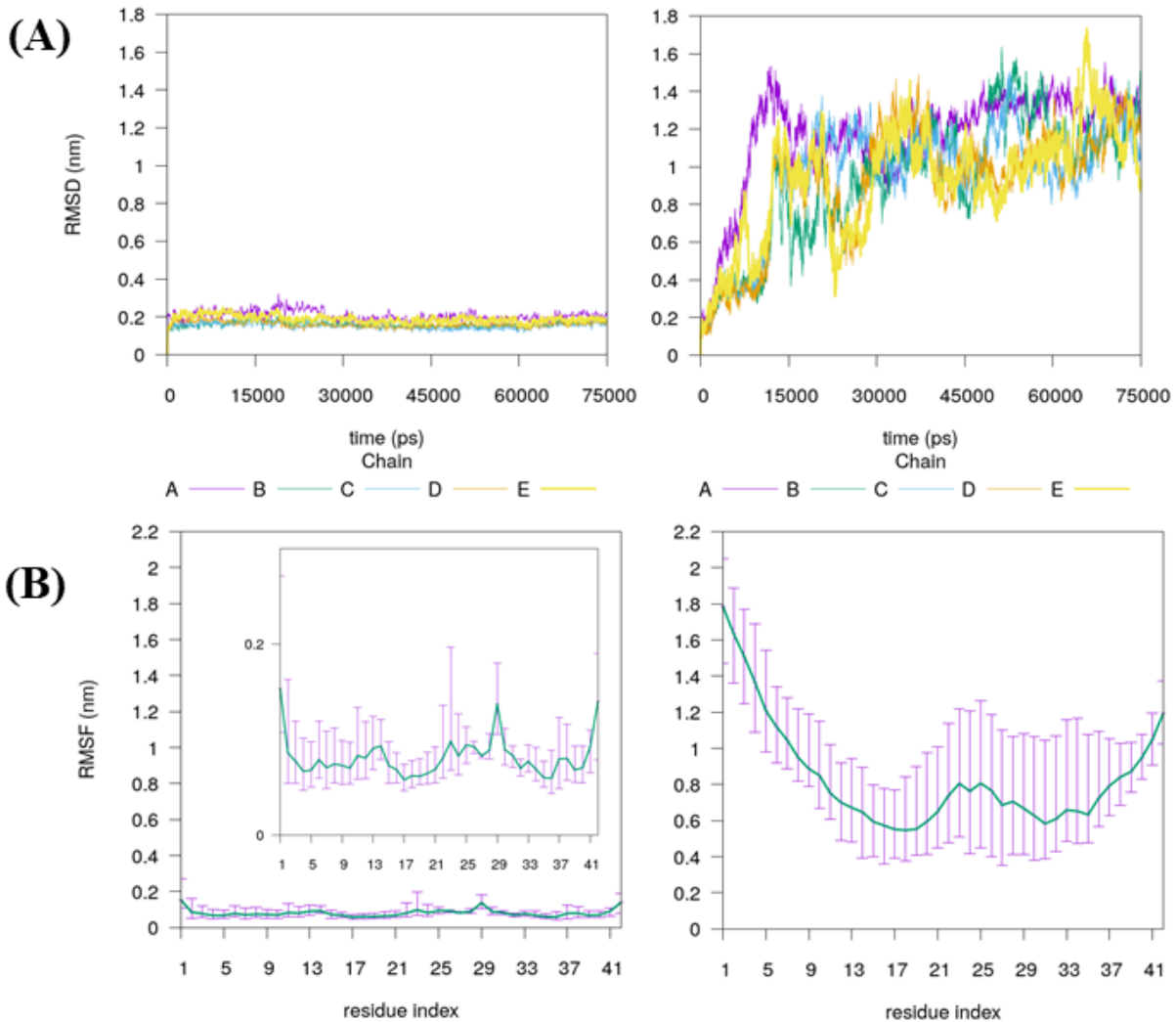


Figure 22: 5OQV- model, (A) Root mean square deviation from initial configuration evaluated on C-alpha for each chain, (B) Root mean square fluctuation averaged on residues (green line) on the wall simulation and range (min,max) (violet bar), moreover for the reference case same data are plotted with a different scale.

Different stability in certain regions can be explained analysing secondary structure probability (Figure 23A) of the two simulated systems. As done in previous literature the probability has been calculated along all chains, for windows of 1 ns, obtaining a time-residue probability. Starting condition for both models show a predominance of rigid  $\beta$ -sheets and flexible coils. Their distribution is the same for both replicas with  $\beta$ -structures situated in three main regions between residues E3-E22, K28-M35 V40-I41. It is possible to observe a noticeable behaviour of the reference system that trough the simulation increase numbers of residues involved in a secondary structure, forming an unique  $\beta$ -sheet region between residue G25-V36. For the second case, shear stress exerted from water molecules drives protein to an unfolded state. Destabilization occurs before in tails regions, in effect around 15 ns  $\beta$ -sheets between regions V39-V40 and G3-T10. Process of destabilization continues, around 50 ns  $\beta$ -sheets region of residues A30-V46 result completely

unstructured. At 75 ns protein completely unfold, losing last  $\beta$ -structure originally formed from residues G11-G22. Moreover, it is possible to observe consistence between results reported from RMSF, (Figure 22B) and this analysis. To deeper understand the process of destabilization, time evolution of contact probability between chain is reported (Figure 23B), in order to understand which residues are involved into non-covalent interaction and where the destabilization process starts. Contact probability is calculated on windows of 1 ns as an average over all pair of chains that are in contact (chains A-B, B-C, C-D, D-D). Both initial configurations show high values of contact probability close to 1. Contact probability evaluated on reference system show high value of contact into all the period of observation. In the case of ultrasound exposure, progressive loss of contact starts from unstructured residues, characterized by higher fluctuations and then propagates to near residues. These seeds of instability behave as starting point for progressive loss of contact between chains.

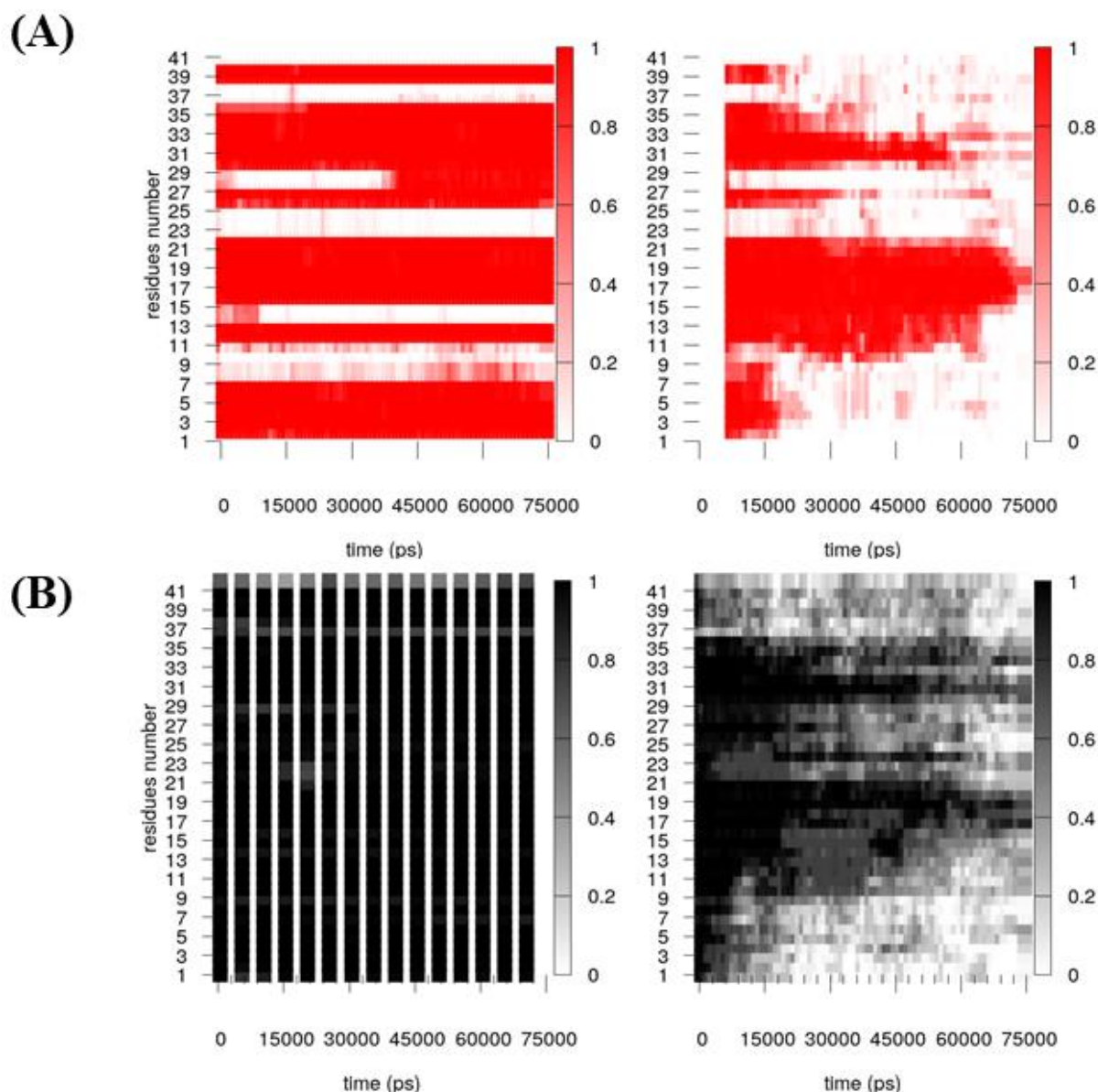


Figure 23: On the left the reference system, on the right the system exposed to ultrasound for 5OQV model. (A) residue secondary structure probability calculated over 5 chains (A-E) every 1 ns. (B) contact probability averaged on each chain in contact (A-B, B-C, C-D, D-E).

## 5.4 Discussion

In this Chapter the “ultrasound” code developed in this work has been employed to perform an analysis of stability for two model of S-shape A $\beta$ 42. These analyses have been performed in order to study another conformation for A $\beta$ 42, the so-called S-shape. In light of the fact that it has been reported this conformation as more stable than U-shape model, analysed in previous chapter. It is worth mentioning that while in U-shape N-terminal residues are believed unstructured and thus omitted in protein model; S-shape models shows a  $\beta$ -sheet conformation for the same residues. Thus, authors suggested that ignoring these residues would results in altering stability of the protein [76], [77]. Inspired by this question two S-shape protein models have been investigated. A first one, pdb

code 2MXU, where residues between E11 to A42 are modelled models, and a second one, pdb code 5OQV, where all residues are considered. Order parameters showed different dynamics of destabilization for 2MXU and 5OQV. Indeed, while the first tend to lose its conformation around 6 ns, the latter need 75 ns of exposure to be destabilized. Comparable results for 2MXU model and 2BEG model, with a lower destabilization dynamics of the first compared to the second are in agreement with the literature [76], [77]. Moreover, it was possible to observe, a tendency from 5OQV to refold (as shown by OrderP plot for 5OQV). Analysis of RMSF shows higher fluctuation for less structured residues. Moreover, while results are comparable for C-terminal residues ( $RMSF_{2MXU-A42}=RMSF_{2MXU-A42=1,2}$ ), region between residues G11-L17 results more stable for the 5OQV. For 5OQV model high value of fluctuation are showed by tails A1-G9 N-terminal residues. Time evolution of secondary structure analysis provides answer to same behaviour of C-terminal residues and the lower mobility for common N-terminal residues of 5OQV model and 2MXU. Indeed, C-terminal are first residues that unfold for both configurations, at different time scale. Different behaviour is showed by residues of N-terminal tail. While in the case of 2MXU residue G11-L17 lose secondary structure contemporary with C-terminal residues, in the 5OQV models results the most stable structure. Time evolution of contact probability provides a description for this different behaviour. Indeed, contact probability analysis showed that unstructured residues act as seed of disaggregation. Thus, higher mobility of N-terminal residue G11-L17 in 2MXU results in augmented tendency to unfold. 5OQV results then stabilized by close  $\beta$ -structure formed by residues, A1-T10, not considered in 2MXU model.

In conclusion this chapter has provided a whole description for A $\beta$ 42 conformation, showing S-shape protein properties, together with U-shape described in previous chapter. Moreover, it has been showed that 5OQV all residues model of S-shape A $\beta$ 42 is more stable than 2MXU model for ultrasound simulations. Thus, ignoring N-terminal residues for this type of simulation would results in a higher tendency to disaggregate for S-shape model.

## 6 Conclusions

Alzheimer disease has been related to aggregation of  $\beta$ -amyloids protein, that starts a cascade of process with result in typical hallmarks of the disease. Many pharmacological strategies have been proposed to counteract this process however they showed to be toxic or ineffective. Ultrasound has a wide range of medical application due to its safeness. Moreover, it has been showed that ultrasound can acts as a natural disaggregates for amyloid plaques. In light of this fact analysing structural stability of protein related to neurodegenerative disease can be promising field of interest.

In this work, an overview of methods reported in literature was carried out to develop a computational “code” to simulate ultrasounds’ effect in molecular dynamics simulations. Strong correlation between results obtained and that reported in literature, provides a robust proof regarding the validity of the code. The methods implemented in this work have been then applied to investigate properties of  $\beta$ -amyloids 1-42. Results provided in this work confirmed that less structured residues tend to show higher fluctuations also in the case of shear stress exerted from water molecules in ultrasound MD simulations. The investigation of amyloid fibril conformational dynamics when excited by ultrasounds has provide information regarding mechanism of stability and protein unfolding. It has been observed that less structured residues, due to the higher fluctuations, acts as seed of instability for the protein. In addition to these results it has been highlighted that molecular models without N-terminal residues are characterized by lower stability. It is worth mention that outcome on N-terminal properties to stabilize S-shape model, emerging from this study, confirmed hypothesis reported in recent work [76].

This work can be seen as starting point to further investigate: 1) effects of ultrasounds on protein conformational behaviour and 2) stability of  $\beta$ -amyloids. In a greater detail, other biological molecules such microtubules have been already considered a possible target for ultrasound applications. The developed code could be employed to investigate molecular characteristics of microtubule polymerization/depolymerization dynamics in present of ultrasounds.

One of the main limitations of method implemented results in a non-physics behaviour of bubbles. Indeed, real cavitation occurs at lower frequency with higher bubble radii. Further studies, with coarse grain models, can be a key to simulate the phenomenon with experimental time and length scales. About stability of  $\beta$ -amyloids under ultrasound exposure, further studies can be performed to shed light on the efficiency of novel synergic strategies characterized for example by a coupled approach ultrasound-inhibitor to affect stability of amyloid aggregates.

## 7 Acknowledgment

Per questo lavoro di tesi vorrei ringraziare:

Il mio relatore Marco Agostino Deriu, per il costante sprono nel cercare di migliorarmi e i continui spunti di riflessione, che mi hanno permesso di ottenere i risultati presentati in questo lavoro.

Il mio co-relatore Umberto Morbiducci, per la revisione critica della tesi.

Stefano Muscat per il supporto alla prima fase dello sviluppo del codice.

Salvatore La Rosa, Marco Castello e Davide Carbonaro per aver condiviso molti momenti durante questo corso di Laurea Magistrale.

Sandy per avermi supportato e sopportato.

I miei genitori, Nunzio e Maria, e le mie sorelle, Elena, e Miriam, per cui non bisogna aggiungere altro motivo.

## 8 Bibliography

- [1] B. L. Miller, W. W. Seeley, P. Mychack, H. J. Rosen, I. Mena, and K. Boone, “Neuroanatomy of the self: Evidence from patients with frontotemporal dementia,” *Neurology*, vol. 57, no. 5, pp. 817–821, Sep. 2001.
- [2] M. J. Prince, “World Alzheimer Report 2015: the global impact of dementia: an analysis of prevalence, incidence, cost and trends,” 2015.
- [3] D. Cantarero-Prieto, P. L. Leon, C. Blazquez-Fernandez, P. S. Juan, and C. S. Cobo, “The economic cost of dementia: A systematic review,” *Dementia*, p. 147130121983777, Mar. 2019.
- [4] W. W. Seeley, R. K. Crawford, J. Zhou, B. L. Miller, and M. D. Greicius, “Neurodegenerative diseases target large-scale human brain networks.,” *Neuron*, vol. 62, no. 1, pp. 42–52, Apr. 2009.
- [5] F. M. Elahi and B. L. Miller, “A clinicopathological approach to the diagnosis of dementia,” *Nat. Rev. Neurol.*, vol. 13, no. 8, pp. 457–476, Aug. 2017.
- [6] P. Marešová, J. Dolejš, and K. Kuca, “Call for a Uniform Strategy of Collecting Alzheimer’s Disease Costs: A Review and Meta-Analysis,” *J. Alzheimer’s Dis.*, vol. 63, no. 1, pp. 227–238, Apr. 2018.
- [7] R. Mahoney, “Anxiety and Depression in Family Caregivers of People With Alzheimer Disease: The LASER-AD Study,” *Am. J. Geriatr. Psychiatry*, vol. 13, no. 9, pp. 795–801, Sep. 2005.
- [8] J. D. Greene, A. D. Baddeley, and J. R. Hodges, “Analysis of the episodic memory deficit in early Alzheimer’s disease: evidence from the doors and people test.,” *Neuropsychologia*, vol. 34, no. 6, pp. 537–51, Jun. 1996.
- [9] B. H. Price, H. Gurvit, S. Weintraub, C. Geula, E. Leimkuhler, and M. Mesulam, “Neuropsychological patterns and language deficits in 20 consecutive cases of autopsy-confirmed Alzheimer’s disease.,” *Arch. Neurol.*, vol. 50, no. 9, pp. 931–7, Sep. 1993.
- [10] C. Esteban-Santillan, R. Praditsuwan, H. Ueda, and D. S. Geldmacher, “Clock drawing test in very mild Alzheimer’s disease.,” *J. Am. Geriatr. Soc.*, vol. 46, no. 10, pp. 1266–9, Oct. 1998.

- [11] V. W. DeLaGarza, "Pharmacologic treatment of Alzheimer's disease: an update.," *Am. Fam. Physician*, vol. 68, no. 7, pp. 1365–72, Oct. 2003.
- [12] "2018 Alzheimer's disease facts and figures," *Alzheimer's Dement.*, vol. 14, no. 3, pp. 367–429, Mar. 2018.
- [13] M. W. Bondi, E. C. Edmonds, and D. P. Salmon, "Alzheimer's Disease: Past, Present, and Future," *J. Int. Neuropsychol. Soc.*, vol. 23, no. 9–10, pp. 818–831, Oct. 2017.
- [14] P. J. Whitehouse, "The cholinergic deficit in Alzheimer's disease.," *J. Clin. Psychiatry*, vol. 59 Suppl 1, pp. 19–22, 1998.
- [15] G. S. Bloom, "Amyloid- $\beta$  and Tau," *JAMA Neurol.*, vol. 71, no. 4, p. 505, Apr. 2014.
- [16] M. P. Murphy and H. LeVine, "Alzheimer's disease and the amyloid-beta peptide.," *J. Alzheimers. Dis.*, vol. 19, no. 1, pp. 311–23, 2010.
- [17] A. Serrano-Pozo, M. P. Frosch, E. Masliah, and B. T. Hyman, "Neuropathological alterations in Alzheimer disease.," *Cold Spring Harb. Perspect. Med.*, vol. 1, no. 1, p. a006189, Sep. 2011.
- [18] C. Haass and D. J. Selkoe, "Soluble protein oligomers in neurodegeneration: Lessons from the Alzheimer's amyloid  $\beta$ -peptide," *Nature Reviews Molecular Cell Biology*, vol. 8, no. 2. pp. 101–112, Feb-2007.
- [19] E. M. Mandelkow and E. Mandelkow, "Tau in Alzheimer's disease.," *Trends Cell Biol.*, vol. 8, no. 11, pp. 425–7, Nov. 1998.
- [20] G. S. Bloom, "Amyloid- $\beta$  and tau: the trigger and bullet in Alzheimer disease pathogenesis.," *JAMA Neurol.*, vol. 71, no. 4, pp. 505–8, Apr. 2014.
- [21] H.-C. Huang and Z.-F. Jiang, "Accumulated amyloid-beta peptide and hyperphosphorylated tau protein: relationship and links in Alzheimer's disease.," *J. Alzheimers. Dis.*, vol. 16, no. 1, pp. 15–27, 2009.
- [22] S. Sarkar, "Neurofibrillary tangles mediated human neuronal tauopathies: insights from fly models.," *J. Genet.*, vol. 97, no. 3, pp. 783–793, Jul. 2018.
- [23] M. P. Mattson, B. Cheng, D. Davis, K. Bryant, I. Lieberburg, and R. E. Rydel, "beta-Amyloid peptides destabilize calcium homeostasis and render human cortical neurons vulnerable to

- excitotoxicity.," *J. Neurosci.*, vol. 12, no. 2, pp. 376–89, Feb. 1992.
- [24] J. Y. Koh, L. L. Yang, and C. W. Cotman, "Beta-amyloid protein increases the vulnerability of cultured cortical neurons to excitotoxic damage.," *Brain Res.*, vol. 533, no. 2, pp. 315–20, Nov. 1990.
- [25] A. Popa-Wagner, E. Schröder, L. C. Walker, and C. Kessler, "β-Amyloid Precursor Protein and β-Amyloid Peptide Immunoreactivity in the Rat Brain After Middle Cerebral Artery Occlusion," *Stroke*, vol. 29, no. 10, pp. 2196–2202, Oct. 1998.
- [26] P. Couratier, M. Lesort, P. Sindou, F. Esclaire, C. Yardin, and J. Hugon, "Modifications of neuronal phosphorylated τ immunoreactivity induced by NMDA toxicity," *Mol. Chem. Neuropathol.*, vol. 27, no. 3, pp. 259–273, Apr. 1996.
- [27] J. Nunan and D. H. Small, "Regulation of APP cleavage by alpha-, beta- and gamma-secretases.," *FEBS Lett.*, vol. 483, no. 1, pp. 6–10, Oct. 2000.
- [28] C. Haass *et al.*, "The Swedish mutation causes early-onset Alzheimer's disease by beta-secretase cleavage within the secretory pathway.," *Nat. Med.*, vol. 1, no. 12, pp. 1291–6, Dec. 1995.
- [29] T. Iwatsubo, "The gamma-secretase complex: machinery for intramembrane proteolysis.," *Curr. Opin. Neurobiol.*, vol. 14, no. 3, pp. 379–83, Jun. 2004.
- [30] G. Chen *et al.*, "Amyloid beta: structure, biology and structure-based therapeutic development," *Acta Pharmacol. Sin.*, vol. 38, no. 9, pp. 1205–1235, Sep. 2017.
- [31] G. G. Glenner and C. W. Wong, "Alzheimer's disease: Initial report of the purification and characterization of a novel cerebrovascular amyloid protein," *Biochem. Biophys. Res. Commun.*, vol. 120, no. 3, pp. 885–890, May 1984.
- [32] M. Coles, W. Bicknell, A. A. Watson, D. P. Fairlie, and D. J. Craik, "Solution Structure of Amyloid β-Peptide(1–40) in a Water–Micelle Environment. Is the Membrane-Spanning Domain Where We Think It Is? † , ‡," *Biochemistry*, vol. 37, no. 31, pp. 11064–11077, Aug. 1998.
- [33] A. T. Petkova *et al.*, "A structural model for Alzheimer's -amyloid fibrils based on experimental constraints from solid state NMR," *Proc. Natl. Acad. Sci.*, vol. 99, no. 26, pp.

16742–16747, Dec. 2002.

- [34] T. Luhrs *et al.*, “3D structure of Alzheimer’s amyloid- (1-42) fibrils,” *Proc. Natl. Acad. Sci.*, vol. 102, no. 48, pp. 17342–17347, Nov. 2005.
- [35] A. T. Petkova, W.-M. Yau, and R. Tycko, “Experimental Constraints on Quaternary Structure in Alzheimer’s  $\beta$ -Amyloid Fibrils †,” *Biochemistry*, vol. 45, no. 2, pp. 498–512, Jan. 2006.
- [36] Y. Xiao *et al.*, “A $\beta$ (1–42) fibril structure illuminates self-recognition and replication of amyloid in Alzheimer’s disease,” *Nat. Struct. Mol. Biol.*, vol. 22, no. 6, pp. 499–505, May 2015.
- [37] L. Gremer *et al.*, “Fibril structure of amyloid- $\beta$ (1–42) by cryo–electron microscopy,” *Science (80-. )*, vol. 358, no. 6359, pp. 116–119, Oct. 2017.
- [38] L. Gu, J. Tran, L. Jiang, and Z. Guo, “A new structural model of Alzheimer’s A $\beta$ 42 fibrils based on electron paramagnetic resonance data and Rosetta modeling,” *J. Struct. Biol.*, vol. 194, no. 1, pp. 61–67, Apr. 2016.
- [39] W. Xi and U. H. E. Hansmann, “Ring-like N-fold Models of A $\beta$ 42 fibrils,” *Sci. Rep.*, vol. 7, no. 1, p. 6588, Dec. 2017.
- [40] W. Xi, W. Wang, G. Abbott, and U. H. E. Hansmann, “Stability of a Recently Found Triple- $\beta$ -Stranded A $\beta$ 1-42 Fibril Motif,” *J. Phys. Chem. B*, vol. 120, no. 20, pp. 4548–4557, 2016.
- [41] A. E. Conicella and N. L. Fawzi, “The C-Terminal Threonine of A $\beta$ 43 Nucleates Toxic Aggregation via Structural and Dynamical Changes in Monomers and Protofibrils,” *Biochemistry*, vol. 53, no. 19, pp. 3095–3105, May 2014.
- [42] T. Härd, “Amyloid Fibrils: Formation, Polymorphism, and Inhibition,” *J. Phys. Chem. Lett.*, vol. 5, no. 3, pp. 607–614, Feb. 2014.
- [43] E. D. EAMES and G. G. GLENNER, “X-RAY DIFFRACTION STUDIES ON AMYLOID FILAMENTS,” *J. Histochem. Cytochem.*, vol. 16, no. 11, pp. 673–677, Nov. 1968.
- [44] M. Sunde and C. C. Blake, “From the globular to the fibrous state: protein structure and structural conversion in amyloid formation.,” *Q. Rev. Biophys.*, vol. 31, no. 1, pp. 1–39, Feb. 1998.

- [45] J. S. Birks, "Cholinesterase inhibitors for Alzheimer's disease," in *Cochrane Database of Systematic Reviews*, J. S. Birks, Ed. Chichester, UK: John Wiley & Sons, Ltd, 2006.
- [46] J. S. Birks and J. Grimley Evans, "Rivastigmine for Alzheimer's disease," in *Cochrane Database of Systematic Reviews*, J. S. Birks, Ed. Chichester, UK: John Wiley & Sons, Ltd, 2015.
- [47] C. W. Wong, "Pharmacotherapy for Dementia: A Practical Approach to the Use of Cholinesterase Inhibitors and Memantine," *Drugs Aging*, vol. 33, no. 7, pp. 451–460, Jul. 2016.
- [48] S. Salomone, F. Caraci, G. M. Leggio, J. Fedotova, and F. Drago, "New pharmacological strategies for treatment of Alzheimer's disease: focus on disease modifying drugs," *Br. J. Clin. Pharmacol.*, vol. 73, no. 4, pp. 504–17, Apr. 2012.
- [49] F. C. Manning, "Tacrine therapy for the dementia of Alzheimer's disease.," *Am. Fam. Physician*, vol. 50, no. 4, pp. 819–26, Sep. 1994.
- [50] M. Weinstock, "Selectivity of Cholinesterase Inhibition," *CNS Drugs*, vol. 12, no. 4, pp. 307–323, 1999.
- [51] J. Birks and R. J. Harvey, "Donepezil for dementia due to Alzheimer's disease.," *Cochrane database Syst. Rev.*, no. 1, p. CD001190, Jan. 2006.
- [52] W. Danysz, C. G. Parsons, H. J. Mobius, A. Stoffler, and G. Quack, "Neuroprotective and symptomatological action of memantine relevant for Alzheimer's disease--a unified glutamatergic hypothesis on the mechanism of action.," *Neurotox. Res.*, vol. 2, no. 2–3, pp. 85–97, 2000.
- [53] R. Briggs, S. P. Kennelly, and D. O'Neill, "Drug treatments in Alzheimers disease," *Clin. Med. (Northfield. Il.)*, vol. 16, no. 3, pp. 247–253, Jun. 2016.
- [54] L. Ghezzi, E. Scarpini, and D. Galimberti, "Disease-modifying drugs in Alzheimer's disease.," *Drug Des. Devel. Ther.*, vol. 7, pp. 1471–8, Dec. 2013.
- [55] S. R. Robinson, G. M. Bishop, H. Lee, and G. Münch, "Lessons from the AN 1792 Alzheimer vaccine: lest we forget," *Neurobiol. Aging*, vol. 25, no. 5, pp. 609–615, May 2004.
- [56] D. A. Loeffler, "Intravenous immunoglobulin and Alzheimer's disease: what now?," *J. Neuroinflammation*, vol. 10, p. 70, Jun. 2013.

- [57] N. D. Prins and P. Scheltens, “Treating Alzheimer’s disease with monoclonal antibodies: current status and outlook for the future.,” *Alzheimers. Res. Ther.*, vol. 5, no. 6, p. 56, 2013.
- [58] R. S. Doody *et al.*, “Phase 3 trials of solanezumab for mild-to-moderate Alzheimer’s disease.,” *N. Engl. J. Med.*, vol. 370, no. 4, pp. 311–21, Jan. 2014.
- [59] S. Salloway *et al.*, “Two phase 3 trials of bapineuzumab in mild-to-moderate Alzheimer’s disease.,” *N. Engl. J. Med.*, vol. 370, no. 4, pp. 322–33, Jan. 2014.
- [60] C. M. Wischik, C. R. Harrington, and J. M. D. Storey, “Tau-aggregation inhibitor therapy for Alzheimer’s disease.,” *Biochem. Pharmacol.*, vol. 88, no. 4, pp. 529–39, Apr. 2014.
- [61] H. Hampel *et al.*, “Lithium trial in Alzheimer’s disease: a randomized, single-blind, placebo-controlled, multicenter 10-week study.,” *J. Clin. Psychiatry*, vol. 70, no. 6, pp. 922–31, Jun. 2009.
- [62] G. Leinenga and J. Götz, “Scanning ultrasound removes amyloid- $\beta$  and restores memory in an Alzheimer’s disease mouse model,” *Sci. Transl. Med.*, vol. 7, no. 278, pp. 278ra33-278ra33, Mar. 2015.
- [63] G. Coppini, G. Valli, and S. Diciotti, *Bioimmagini*, 2002nd ed. Bologna, 202AD.
- [64] S. B. Jun, “Ultrasound as a noninvasive neuromodulation tool,” *Biomed. Eng. Lett.*, vol. 2, no. 1, pp. 8–12, Mar. 2012.
- [65] V. Y. T. Cheung, “High-intensity focused ultrasound therapy,” *Best Practice and Research: Clinical Obstetrics and Gynaecology*, vol. 46. Baillière Tindall, pp. 74–83, 01-Jan-2018.
- [66] R. M. Nisbet and J. Götz, “Amyloid- $\beta$  and Tau in Alzheimer’s Disease: Novel Pathomechanisms and Non-Pharmacological Treatment Strategies,” *J. Alzheimer’s Dis.*, vol. 64, no. s1, pp. S517–S527, Jun. 2018.
- [67] J. F. Jordão *et al.*, “Amyloid- $\beta$  plaque reduction, endogenous antibody delivery and glial activation by brain-targeted, transcranial focused ultrasound.,” *Exp. Neurol.*, vol. 248, pp. 16–29, Oct. 2013.
- [68] G. Leinenga, C. Langton, R. Nisbet, and J. Götz, “Ultrasound treatment of neurological diseases — current and emerging applications,” *Nat. Rev. Neurol.*, vol. 12, no. 3, pp. 161–174, Mar. 2016.

- [69] H. Yagi, K. Hasegawa, Y. Yoshimura, and Y. Goto, “Acceleration of the depolymerization of amyloid  $\beta$  fibrils by ultrasonication,” *Biochim. Biophys. Acta - Proteins Proteomics*, vol. 1834, no. 12, pp. 2480–2485, Dec. 2013.
- [70] M. Karplus and J. Kuriyan, “Molecular dynamics and protein function,” *Proc. Natl. Acad. Sci.*, vol. 102, no. 19, pp. 6679–6685, May 2005.
- [71] M. Karplus, “Molecular Dynamics Simulations of Biomolecules,” *Acc. Chem. Res.*, vol. 35, no. 6, pp. 321–323, Jun. 2002.
- [72] M. Hassan, S. Shahzadi, S. Y. Seo, H. Alashwal, N. Zaki, and A. A. Moustafa, “Molecular Docking and Dynamic Simulation of AZD3293 and Solanezumab Effects Against BACE1 to Treat Alzheimer’s Disease,” *Front. Comput. Neurosci.*, vol. 12, Jun. 2018.
- [73] G. Kryger, I. Silman, and J. L. Sussman, “Structure of acetylcholinesterase complexed with E2020 (Aricept®): implications for the design of new anti-Alzheimer drugs,” *Structure*, vol. 7, no. 3, pp. 297–307, Mar. 1999.
- [74] M. López de la Paz, G. M. S. de Mori, L. Serrano, and G. Colombo, “Sequence Dependence of Amyloid Fibril Formation: Insights from Molecular Dynamics Simulations,” *J. Mol. Biol.*, vol. 349, no. 3, pp. 583–596, Jun. 2005.
- [75] B. Urbanc *et al.*, “Molecular dynamics simulation of amyloid beta dimer formation,” *Biophys. J.*, vol. 87, no. 4, pp. 2310–21, Oct. 2004.
- [76] G. Grasso *et al.*, “Conformational Dynamics and Stability of U-Shaped and S-Shaped Amyloid  $\beta$  Assemblies,” *Int. J. Mol. Sci.*, vol. 19, no. 2, p. 571, Feb. 2018.
- [77] G. Grasso, M. Rebella, U. Morbiducci, J. A. Tuszynski, A. Danani, and M. A. Deriu, “The Role of Structural Polymorphism in Driving the Mechanical Performance of the Alzheimer’s Beta Amyloid Fibrils,” *Front. Bioeng. Biotechnol.*, vol. 7, Apr. 2019.
- [78] C. E. Brennen and N. Y. Oxford, “Cavitation and Bubble Dynamics,” 1995.
- [79] M. Hoang Viet, P. Derreumaux, and P. H. Nguyen, “Nonequilibrium all-atom molecular dynamics simulation of the bubble cavitation and application to dissociate amyloid fibrils,” *J. Chem. Phys.*, vol. 145, no. 17, p. 174113, Nov. 2016.
- [80] H. van de Waterbeemd *et al.*, “Glossary of terms used in computational drug design (IUPAC

Recommendations 1997),” *Pure Appl. Chem.*, vol. 69, no. 5, pp. 1137–1152, Jan. 1997.

- [81] G. A. Worth and L. S. Cederbaum, “BEYOND BORN-OPPENHEIMER: Molecular Dynamics Through a Conical Intersection,” *Annu. Rev. Phys. Chem.*, vol. 55, no. 1, pp. 127–158, Jun. 2004.
- [82] Jacob Chapman, “Improving the Functional Control of Ferroelectrics using Insights from Atomistic modelling - Scientific Figure on ResearchGate.” .
- [83] H. LIN, B. D. STOREY, and A. J. SZERI, “Inertially driven inhomogeneities in violently collapsing bubbles: the validity of the Rayleigh–Plesset equation,” *J. Fluid Mech.*, vol. 452, pp. 145–162, Feb. 2002.
- [84] V. H. Man, M. S. Li, P. Derreumaux, and P. H. Nguyen, “Rayleigh-Plesset equation of the bubble stable cavitation in water: A nonequilibrium all-atom molecular dynamics simulation study,” *J. Chem. Phys.*, vol. 148, no. 9, p. 094505, Mar. 2018.
- [85] C. A. Ross and M. A. Poirier, “Protein aggregation and neurodegenerative disease,” *Nat. Med.*, vol. 10, no. S7, pp. S10–S17, Jul. 2004.
- [86] A. Mullard, “Anti-amyloid failures stack up as Alzheimer antibody flops,” *Nat. Rev. Drug Discov.*, Apr. 2019.
- [87] D. Mehta, R. Jackson, G. Paul, J. Shi, and M. Sabbagh, “Why do trials for Alzheimer’s disease drugs keep failing? A discontinued drug perspective for 2010-2015,” *Expert Opin. Investig. Drugs*, vol. 26, no. 6, pp. 735–739, Jun. 2017.
- [88] M. C. Peek and F. Wu, “High-intensity focused ultrasound in the treatment of breast tumours,” *Ecancermedicalscience*, vol. 12, Jan. 2018.
- [89] E. Maloney and J. H. Hwang, “Emerging HIFU applications in cancer therapy,” *Int. J. Hyperth.*, vol. 31, no. 3, pp. 302–309, Apr. 2015.
- [90] A. Samarbakhsh and J. A. Tuszynski, “Resonance condition in microtubules using ultrasound plane waves,” *J. Comput. Theor. Nanosci.*, vol. 9, no. 1, pp. 67–71, 2012.
- [91] B. Liu, H. Ma, S. Li, W. Zhao, and L. Li, “[Study on the effect of ultrasound on the secondary structure of BSA by FTIR].,” *Guang Pu Xue Yu Guang Pu Fen Xi*, vol. 30, no. 8, pp. 2072–6, Aug. 2010.

- [92] M. Karplus and J. A. McCammon, "Molecular dynamics simulations of biomolecules," *Nat. Struct. Biol.*, vol. 9, no. 9, pp. 646–652, Sep. 2002.
- [93] K. Koshiyama, T. Kodama, T. Yano, and S. Fujikawa, "Molecular dynamics simulation of structural changes of lipid bilayers induced by shock waves: Effects of incident angles," *Biochim. Biophys. Acta - Biomembr.*, vol. 1778, no. 6, pp. 1423–1428, Jun. 2008.
- [94] C. Sagui and T. A. Darden, "Molecular dynamics simulations of biomolecules: long-range electrostatic effects.," *Annu. Rev. Biophys. Biomol. Struct.*, vol. 28, pp. 155–79, 1999.
- [95] H. J. C. Berendsen, D. van der Spoel, and R. van Drunen, "GROMACS: A message-passing parallel molecular dynamics implementation," *Comput. Phys. Commun.*, vol. 91, no. 1–3, pp. 43–56, Sep. 1995.
- [96] J. Nasica-Labouze *et al.*, "Amyloid  $\beta$  Protein and Alzheimer's Disease: When Computer Simulations Complement Experimental Studies," *Chem. Rev.*, vol. 115, no. 9, pp. 3518–3563, May 2015.
- [97] K. Lindorff-Larsen *et al.*, "Improved side-chain torsion potentials for the Amber ff99SB protein force field.," *Proteins*, vol. 78, no. 8, pp. 1950–8, Jun. 2010.
- [98] G. Bussi, D. Donadio, and M. Parrinello, "Canonical sampling through velocity rescaling," *J. Chem. Phys.*, vol. 126, no. 1, p. 014101, Jan. 2007.
- [99] D. Frishman and P. Argos, "Knowledge-based protein secondary structure assignment.," *Proteins*, vol. 23, no. 4, pp. 566–79, Dec. 1995.
- [100] M. Cheon, C. K. Hall, and I. Chang, "Structural Conversion of A $\beta$ 17–42 Peptides from Disordered Oligomers to U-Shape Protofilaments via Multiple Kinetic Pathways," *PLoS Comput. Biol.*, vol. 11, no. 5, p. e1004258, May 2015.
- [101] N. McDannold, N. Vykhodtseva, and K. Hynynen, "Effects of Acoustic Parameters and Ultrasound Contrast Agent Dose on Focused-Ultrasound Induced Blood-Brain Barrier Disruption," *Ultrasound Med. Biol.*, vol. 34, no. 6, pp. 930–937, Jun. 2008.
- [102] L. Gremer *et al.*, "Fibril structure of amyloid- $\beta$ (1-42) by cryo-electron microscopy.," *Science*, vol. 358, no. 6359, pp. 116–119, 2017.
- [103] R. Dal Magro *et al.*, "The Extent of Human Apolipoprotein A-I Lipidation Strongly Affects

the  $\beta$ -Amyloid Efflux Across the Blood-Brain Barrier in vitro,” *Front. Neurosci.*, vol. 13, May 2019.

- [104] M. A. Deriu *et al.*, “Characterization of the AXH domain of Ataxin-1 using enhanced sampling and functional mode analysis,” *Proteins Struct. Funct. Bioinforma.*, vol. 84, no. 5, pp. 666–673, May 2016.
- [105] G. Grasso, M. A. Deriu, J. A. Tuszynski, D. Gallo, U. Morbiducci, and A. Danani, “Conformational fluctuations of the AXH monomer of Ataxin-1,” *Proteins Struct. Funct. Bioinforma.*, vol. 84, no. 1, pp. 52–59, Jan. 2016.
- [106] G. Grasso, U. Morbiducci, D. Massai, J. Tuszynski, A. Danani, and M. Deriu, “Destabilizing the AXH Tetramer by Mutations: Mechanisms and Potential Antiaggregation Strategies,” *Biophys. J.*, vol. 114, no. 2, pp. 323–330, 2018.